This material may be protected by Copyright law (Title 17 U.S. Code)

Handbook of Spintronics
DOI 10.1007/978-94-007-7604-3_35-1
© Springer Science+Business Media Dordrecht 2014

# Physics and Design of Hard Disk Drive Magnetic Recording Read Heads

Stefan Maat* and Arley C. Marley
Magnetic Recording Heads Development, HGST, a Western Digital Company, San Jose, CA, USA

## Abstract

Magnetic recording heads always have been on the forefront of technology. A finished magnetic recording head that is manufactured in high volume is the outcome of a coordinated effort of various scientific and engineering disciplines. This chapter will focus on the physics and design of modern magnetic recording read heads. It will explain the underlying concepts of thin film magnetism and electron transport in nanostructures and describe the aspects of device scaling, magnetic stabilization, signal-to-noise considerations, and read-back performance of currently employed tunnel magnetoresistive read heads. An outlook on possible future read-head technologies such as current-perpendicular-to-the-plane giant magnetoresistance, scissor, two-dimensional magnetic recording, and spin-torque sensors will be given.

## List of Abbreviations

| | |
|---|---|
| **α** | Magnetic damping constant |
| **β** | Bulk spin-scattering parameter |
| **γ** | Interface spin-scattering parameter |
| **Θ** | Angle of layer magnetization with respect to the magnetic field |
| **a** | Media transition length |
| **ABS** | Air-bearing surface |
| **ACL** | Antiferromagnetic coupling layer |
| **AF** | Antiferromagnet |
| **AMR** | Anisotropic magnetoresistance |
| **bcc** | Body-centered cubic |
| **BP** | Bias point |
| **CFAS** | $Co_2Fe_{0.5}Al_{0.5}Si$ |
| **CIP** | Current in plane |
| **CL** | Cap layer |
| **CMP** | Chemical mechanical polishing |
| **CPP** | Current perpendicular to the plane |
| **FL** | Free layer |
| **g** | Gyromagnetic ratio |
| **GBit/in$^2$** | Gigabit/square inch |
| **GMR** | Giant magnetoresistance |
| **H** | Magnetic field |
| **$H_\perp$** | Magnetic out-of-plane stiffness field |

*Email: stefan.maat@hgst.com



IP Bridge Exhibit 2038
Western Digital v. IP Bridge
IPR2024-01447

DOI 10.1007/978-94-007-7604-3_35-1
© Springer Science+Business Media Dordrecht 2014

| | |
|---|---|
| **hcp** | Hexagonal close packed |
| $\mathbf{H_D}$ | Demagnetization field |
| $\mathbf{H_{HB}}$ | Hard-bias field |
| $\mathbf{H_{II}}$ | Magnetic in-plane stiffness field |
| **HMS** | Head-media spacing |
| **IBD** | Ion beam deposition |
| **IBM** | International Business Machines |
| $\mathbf{k_B}$ | Boltzmann constant |
| $\mathbf{l_{SF}}$ | Spin-diffusion length |
| $\mathbf{M_F}$ | Free layer magnetization |
| **MR** | Magnetoresistance |
| $\mathbf{M_r}$ | Remanent magnetization |
| **MRW** | Magnetic read width |
| $\mathbf{M_s}$ | Saturation magnetization |
| **OTC** | Offtrack capability |
| **OTP** | Offtrack position |
| **P** | Spin polarization |
| **PL** | Pinned layer |
| **PVD** | Physical vapor deposition |
| **PW** | Pulse width |
| **R** | Resistance |
| $\mathbf{R_0}$ | Sensor resistance at zero field |
| **RA** | Resistance-area product |
| $\mathbf{R_{AC}}$ | Alternating current resistance |
| $\mathbf{R_{AP}}$ | Sensor resistance in the antiparallel state |
| $\mathbf{R_{DC}}$ | Direct current resistance |
| **RG** | Read gap |
| $\mathbf{R_{Hmax}}$ | Sensor resistance for negative media field |
| $\mathbf{R_{Hmin}}$ | Sensor resistance for positive media field |
| **RKKY** | Ruderman-Kittel-Kasuya-Yosida |
| **RL** | Reference layer |
| $\mathbf{R_P}$ | Sensor resistance in the parallel state |
| **S** | Noise spectral density |
| **S1** | Bottom shield |
| **S2** | Top shield |
| **SH** | Stripe height |
| **SL** | Seed layer |
| **SNR** | Signal-to-noise ratio |
| **SQTP** | Squeeze track pitch |
| **SSS** | Shield-to-shield spacing |
| **T** | Absolute temperature in Kelvin |
| **t** | Thickness |
| **TB** | Tunnel barrier |
| **TDMR** | Two-dimensional magnetic recording |
| **TFC** | Thermal flight-height control |
| **TMR** | Tunnel magnetoresistance |
| **TW** | Track width |

DOI 10.1007/978-94-007-7604-3_35-1
© Springer Science+Business Media Dordrecht 2014

| | |
|---|---|
| **u** | Utilization |
| $\mathbf{V_b}$ | Bias voltage |
| $\mathbf{V_F}$ | Free layer volume |

## Introduction: Scaling of Magnetic Recording

Magnetic recording read heads have come a long way since the introduction of magnetic disk drive technology by IBM in 1957. Since then, recording densities increased from 2 kBit/in$^2$ to about 750 GBit/in$^2$ in the year 2011. The aggressive exponential growth in areal density, which was mainly achieved by reducing the size of the written bits on the disk, required not only the size of the read sensor to shrink accordingly but also frequent changes in reader technology. While some of the changes seem to be incremental such as the gradual reduction in sensor dimensions and the ongoing improvement in materials, others involved a complete change in reader technology taking advantage of newly discovered physical effects, which offered better read-head signal-to-noise ratios as reader scaling continued.

Thus, over the years, magnetic recording head technology has evolved from bulk inductive heads with wire-wound coils in the early years of magnetic recording to lithographically defined thin film inductive heads in 1979 to anisotropic magnetoresistance (AMR) read heads in 1991 to current-in-plane giant magnetoresistance (CIP-GMR) read heads in 1996 and most recently to tunnel magnetoresistance (TMR) read heads in 2006. With the evolution of the recording technology, the areal recording density has increased dramatically as shown in Fig. 1. Frequently, a change in areal density compound growth rate was observed with the introduction with a new recording technology most notable from 25 % to 60 % and then 100 % with the introduction of AMR and CIP-GMR heads, respectively. More recently, the areal density growth rate has slowed down to 40 % and 25 % again due to increasingly higher technology challenges. Besides the improvement in recording head technology, other notable improvements such as the introduction of antiferromagnetically coupled media in 2000 and the switch from longitudinal to perpendicular recording in 2002 are also shown.

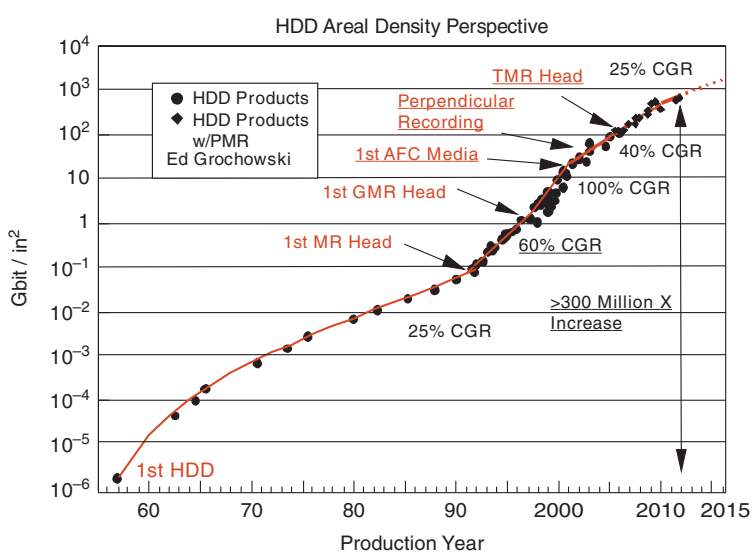


**Fig. 1** Compound growth rate (*CGR*) in areal recording density by year (Reprinted with permission from Ref. [1]. © Copyright June 2012 Coughlin Associates)

Handbook of Spintronics
DOI 10.1007/978-94-007-7604-3_35-1
© Springer Science+Business Media Dordrecht 2014

**Table 1** Evolution of read-sensor technology, the year of product introduction, recording density, sensor geometry, magnetoresistance effect, structure, and current geometry is shown (*CIP* current in plane, *CPP* current perpendicular to the plane of the sensor)

| Year | Sensor technology | MR effect | 1st density | Current geometry | Structure | Typical MR |
|---|---|---|---|---|---|---|
| 1979 | Thin film inductive | N/A | 0.01 Gb/in$^2$ | N/A | 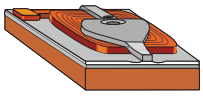 | N/A |
| 1991 | MR sensor | Anisotropic MR | 0.1 Gb/in$^2$ | **CIP** | 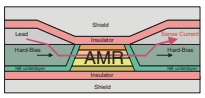 | **2** % |
| 1996 | Spin valve | Giant MR | 2 Gb/in$^2$ | **CIP** | 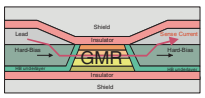 | **15** % |
| 2006 | Tunnel valve | Tunneling MR | 100 Gb/in$^2$ | **CPP** | 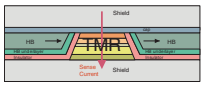 | **50** %<br>**1 Ω-μm$^2$** |
| ? | CPP-GMR | Giant MR | >1 Tb/in$^2$ | **CPP** | 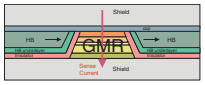 | **10** %<br>**50 mΩ-μm$^2$** |

Table 1 gives a more detailed overview of the stages in read-head technology. Listed in the first to seventh columns are the year of commercial introduction, the sensor technology, the MR effect, the first density, the current geometry, a typical reader structure, and a typical MR, respectively.

The AMR is a bulk effect which is attributed to preferential scattering of s-d electrons in the direction of the applied magnetic field. Thus, the electrical resistance in most magnetic materials is highest field and current are parallel to each other, while it is lowest when they are perpendicular to each other. Typical signals in AMR read heads were only around 2 %. This is why the discovery of the giant magnetoresistive effect (GMR) by the groups of Peter Grünberg [2] and Albert Fert [3] in 1988 sparked a lot of attention. The initial discovery was made in Fe/Cr multilayers, and a GMR of up to 50 % in high fields and at low temperature was reported but soon after the effect was also observed in Co/Cu and CoFe/Cu multilayers [4] and was finally utilized in the form of CIP spin valves [5–7] featuring a magnetic sense and reference layer structure. While the sense layer magnetization is free to rotate in the field of the magnetic bits, the reference layer magnetization is fixed by being exchange biased by an antiferromagnet. Initially, CIP spin-valve structures only exhibited ∼2 % room-temperature GMR, but eventually, GMR values exceeding 15 % were achieved utilizing specularly reflective oxide layers [8]. For the discovery of the GMR effect, Fert and Grünberg were awarded the Nobel Prize in Physics in 2007. With further shrinking sensor dimensions and the advent of low resistance-area MgO tunnel barriers, the industry transitioned to TMR sensors in 2006, which now easily exhibit >50 % TMR. While the sense current for AMR and CIP-GMR head technologies was flowing parallel to the plane of a photolithographically defined stack of multilayers, the sense current in present-day TMR heads flows perpendicular to the plane of the stack. Thus, a TMR sensor is also referred to as a current-perpendicular-to-the-plane (CPP)

Handbook of Spintronics
DOI 10.1007/978-94-007-7604-3_35-1
© Springer Science+Business Media Dordrecht 2014

sensor, while the previous sensors are referred to as CIP sensors. Further technology changes may be required in the near or more distant future, depending on how aggressively scaling continues. Some of the technologies on the horizon are CPP-GMR, bilayer scissor sensors, or spin-torque oscillators. Many comprehensive research papers, reviews [9, 10], and book chapters [11] have been written over the years on AMR and CIP-GMR sensors as the reader technology evolved, and so this chapter will focus only on present and promising future technologies. Here, it will be explained how a modern TMR sensor operates, is built, and is tested and what design constraints are considered to obtain a stable read head with adequate signal-to-noise ratio (SNR). Finally, an outlook on new technologies and what may trigger a migration to these technologies will be given.

## Growth and Processing of Tunneling Magnetoresistance Sensors

The tunnel magnetoresistance (TMR) effect utilized in the present-day recording heads is purely quantum mechanical in nature. Spin-polarized electrons tunnel from one magnetic electrode (F1) through a thin insulating layer (I) into another magnetic electrode (F2). A simplistic model describing the effect was first developed by Julliere [12]. In this model the tunneling process is described by a parallel current path model for spin-up and spin-down electrons where only the polarization of the ferromagnetic electrode materials rather than their detailed band-structure is taken into account. Moreover, no spin-flip scattering or barrier height dependence is considered. Thus, the Julliere model is generally not appropriate to describe spin-dependent tunneling [13]. In the case of the Julliere model, the tunneling process is described by a parallel current path model for spin-up and spin-down electrons.

The polarization of a magnetic material is defined as $P = \frac{D_\uparrow(E_F) - D_\downarrow(E_F)}{D_\uparrow(E_F) + D_\downarrow(E_F)}$, where $D_{\uparrow/\downarrow}(E_F)$ are the density of states of the spin-up (↑) and spin-down (↓) electrons at the Fermi level, respectively. Thus, a half-metal, where one spin channel exhibits a gap at the Fermi energy while the other one is populated, exhibits 100 % spin polarization. The quest for highly spin-polarized and half-metallic materials currently is a field of intense research. While $CrO_2$ was shown to be highly spin polarized at low temperature [14], this material is not of practical importance as its Curie temperature of 390 K is very low [15]. More promising materials are various types of Heusler compounds, which are half-metallic in the partially (B2) or fully ($L2_1$) chemically ordered state and also exhibit high Curie temperatures [16]. A high degree of chemical order, however, is difficult to realize at growth temperatures <300 ºC compatible with processing of magnetic recording heads. For a lower degree of chemical order, defect states develop in the bandgap due to imperfections, which effectively decrease the spin polarization [17]. The tunneling process for the parabolic bands of free electrons is shown in Fig. 2. If no voltage is applied across the F1/I/F2 junction, electrons tunnel in each direction with equal probability. If a positive bias voltage, $V_b$, is applied, electrons tunnel from F1 to F2. For parallel F1 and F2 magnetizations as shown in Fig. 2a, the tunneling probability is high as the same number of initial and final states for both spin-up and spin-down electrons is available. For antiparallel F1 and F2 magnetizations as shown in Fig. 2b, the tunneling probability is low since the number of available initial and final states is reduced.

The TMR within the Julliere model is described by

$$\mathrm{TMR} = \frac{2P_1P_2}{1 - P_1P_2} \tag{1}$$

DOI 10.1007/978-94-007-7604-3_35-1
© Springer Science+Business Media Dordrecht 2014

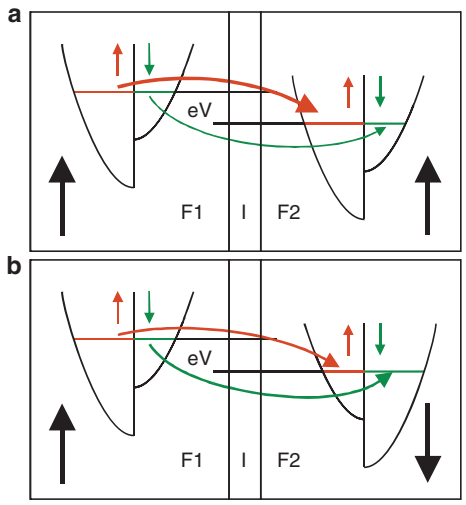


**Fig. 2** F1/I/F2 tunnel junction: electrons have (**a**) a high probability of tunneling in the parallel and (**b**) a low probability in the antiparallel configuration

where the TMR increases with spin polarization and is infinite at 100 % spin polarization. Despite the shortcomings of the Julliere model, it was frequently used to describe TMR in early junctions with $Al_2O_3$ as it was able to qualitatively describe the tunneling process.

Early studies of tunnel magnetoresistance junctions mostly involved an amorphous $Al_2O_3$ tunnel barrier with magnetic transition metal electrodes such as Co and NiFe as it was possible to obtain >10 % TMR values at room temperature [18, 19]. To describe the tunneling process in these junctions, the Julliere model is applicable. $Al_2O_3$ tunnel junctions, however, were never implemented into recording heads due to the advent of low resistance MgO tunnel barriers exhibiting much higher TMR values. Recently, much higher room-temperature TMR values were realized using Heusler alloys as bottom electrodes of $Al_2O_3$ tunnel junctions [20–22]. However, in all these cases, the thickness of these Heusler alloy layers is much too thick for any application in a recording head.

In 2001, the groups of Butler [23] and Mathon [24] independently predicted high TMR for Fe/MgO/Fe tunnel junctions with (001) crystallographic orientation utilizing first-principles calculations. The origin of the large TMR effect in this system can only be explained by detailed band-structure calculations. The MgO tunnel barrier acts as a spin filter for the spin-polarized electrons of a certain symmetry, and thus the above-mentioned simplistic Julliere model cannot be applied. For coherent tunneling, only electrons with wave functions exhibiting axial symmetry normal to the plane of the barrier are considered. Most importantly, the Fe majority $\Delta_1$ (spd) electrons decay as evanescent waves with same symmetry in the MgO and thus can effectively tunnel from one electrode into the other electrode for parallel state resulting in a high conductivity. The Fe majority $\Delta_2$' (d) and $\Delta_5$ (pd) electrons are filtered out effectively by the MgO barrier. There are no Fe minority $\Delta_1$ (spd) states available at the Fermi level, and the Fe minority $\Delta_2$ (d), $\Delta_2$' (d), and $\Delta_5$ (pd) electrons are filtered out effectively by the MgO barrier, resulting in a low conductivity in the antiparallel state. In practice, materials and interfaces are never perfect, and some coherency is lost resulting in a lower TMR than calculated.

In 2004, additional theoretical studies also predicted large TMR for bcc Co/MgO/Co and FeCo/MgO/FeCo [25], and large TMR was indeed observed in tunnel junctions with (001) textured

DOI 10.1007/978-94-007-7604-3_35-1
© Springer Science+Business Media Dordrecht 2014

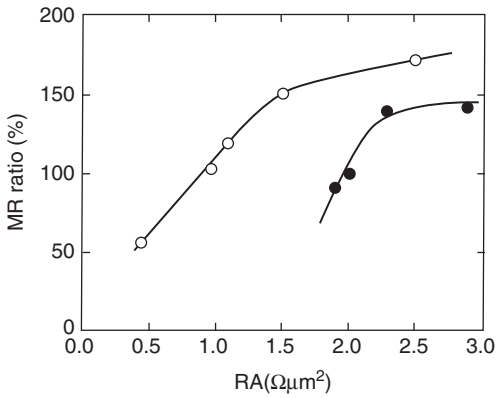


**Fig. 3** MR ratio versus RA plot for CoFeB/MgO/CoFeB tunnel junctions at room temperature. Lower RA product corresponds to a thinner barrier. The TMR decreases as the barrier thickness is decreased due to imperfections of the barrier (Reprinted with permission from Ref. [29]. Copyright (2006), AIP Publishing LLC)

$CoFe_{16}$/Fe/MgO/$CoFe_{30}$ and $CoFe_{30}$/MgO/$CoFe_{16}$ [26] and fully epitaxial Fe(001)/MgO(001)/Fe (001) films [27].

For read-head applications, however, the MgO barriers used in the above-cited work were either very thick resulting in high resistance-area (RA) values or fully epitaxial grown on single-crystal substrates, which is incompatible with read-head manufacturing where junctions are grown by sputtering on plated magnetic shields. However, in 2005, Djayaprawira et al. found that high TMR can also be achieved with a CoFeB/MgO/CoFeB system [28] in which the amorphous CoFeB layer promotes a strong (001) textured growth of the MgO. Later, Nagamine et al. [29] showed that >50 % TMR at 0.4 $\Omega\mu m^2$ can be achieved for CoFeB/MgO/CoFeB. This enabled the use of MgO barriers in magnetic recording read heads. A typical TMR-RA plot of a CoFeB/MgO/CoFeB tunnel junction is shown in Fig. 3. The intrinsically high MR of MgO at low RA products has boosted the read-head performance by providing significantly higher read-back signals (amplitude) compared to earlier thin film technologies. The TMR in CoFe(B)/MgO/CoFe(B) tunnel junctions strongly varies with Co-Fe composition [30]. It initially increases as Co is added to Fe, but then decreases beyond a certain composition. The exact location of the peak depends on the thickness of the layers and preparation of the structure. A recent study comparing transport and spin-resolved photoemission experiments on epitaxially grown $Co_xFe_{1-x}$/MgO/$Co_xFe_{1-x}$ tunnel junctions showed that the TMR drops due to the appearance of a minority $\Delta_1$ interface state above $x > 0.25$ and bulk empty minority $\Delta_1$ states crossing the Fermi level for $x > 0.5$ [31].

A schematic view of a typical TMR stack is shown in Fig. 4. A TMR stack comprises a seed layer (SL), an antiferromagnet (AF), a pinned layer (PL), an antiferromagnetic coupling layer (ACL), a reference layer (RL), a tunnel barrier (TB), a free layer (FL), and a cap layer (CL) and is located between a bottom (S1) and a top magnetic shield (S2). Prior to the growth of the sensor stack, the S1 surface is smoothened by chemical mechanical polishing (CMP). The TMR sensor stack is deposited by magnetron sputtering also often referred to as physical vapor deposition (PVD) onto the bottom shield (S1). After formation of the tunnel junction, the top shield (S2) is deposited onto the TMR stack. The distance from S1 to S2 is called the shield-to-shield spacing (SSS) and is one of the quantities defining sensor's ability to resolve the signal from individual bits.

The shields are commonly made of electroplated NiFe alloy films as they need to exhibit a high magnetic permeability to shield the read head from the field of the write pole and bits of the disk which are outside the read gap and should not be detected by the sensor.

DOI 10.1007/978-94-007-7604-3_35-1
© Springer Science+Business Media Dordrecht 2014

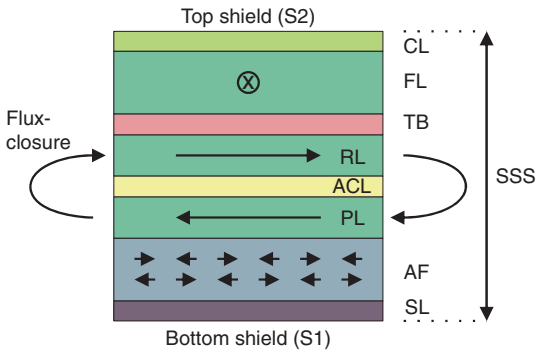


**Fig. 4** Schematic view of a TMR stack comprising a seed layer (*SL*), an antiferromagnet (*AF*), a pinned layer (*PL*), an antiferromagnetic coupling layer (*ACL*), a reference layer (*RL*), a tunnel barrier (*TB*), a free layer (*FL*), and a cap layer (*CL*). The stack is deposited onto a bottom magnetic shield (*S1*). A top magnetic shield (*S2*) is deposited onto the TMR stack. The distance between bottom and top shields is called the shield-to-shield spacing (*SSS*). The hard bias stabilizing the free layer is not shown

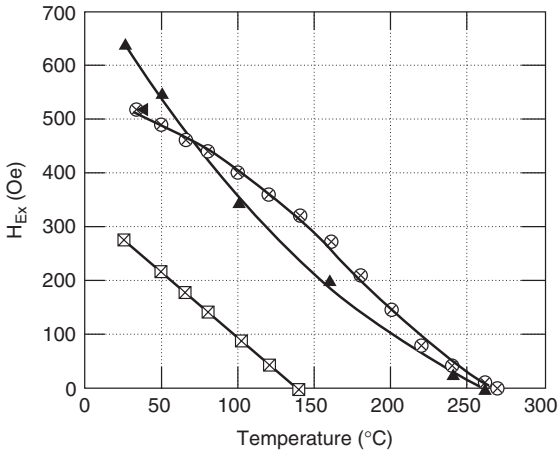


**Fig. 5** Temperature dependence of unidirectional anisotropy $H_{ex}$ for as-deposited and annealed Ta(5 nm)/AF/$Co_{90}Fe_{10}$(2 nm)/Cu(3 nm)/$Co_{90}Fe_{10}$(3 nm)/NiFe(2 nm)/CoZrNb(10 nm) films on AlOx-coated Si substrates. *Triangles*: as-deposited structure with AF = IrMn(8 nm). *Circles*: annealed structure with AF = IrMn(8 nm). *Squares*: as-deposited structure with AF = FeMn(15 nm) (Reprinted with permission from Ref. [33]. Copyright (1997), AIP Publishing LLC)

While the free layer is generally free to change its magnetization direction in response to small external magnetic fields, the reference layer remains generally stable against these small field disturbances. This is achieved by depositing the reference layer as part of a pinned layer structure on top of an antiferromagnet and inducing a unidirectional anisotropy by exchange biasing the pinned layer structure by means of subsequent field annealing. The unidirectional anisotropy induced by the exchange bias manifests itself by a shift of the pinned layer structure hysteresis loop (for a review on exchange biasing, see, e.g., Nogues et al. [32]).

The antiferromagnetic layer used in a TMR stack typically is $\sim Ir_{20}Mn_{80}$ as it can be grown very thin and provides high exchange strength and high blocking temperatures in excess of 250 ºC [33–35]. The exact composition will depend on the pinned layer material and composition. The blocking temperature is defined as the temperature where the exchange bias is reduced to zero, i.e.,

DOI 10.1007/978-94-007-7604-3_35-1
© Springer Science+Business Media Dordrecht 2014

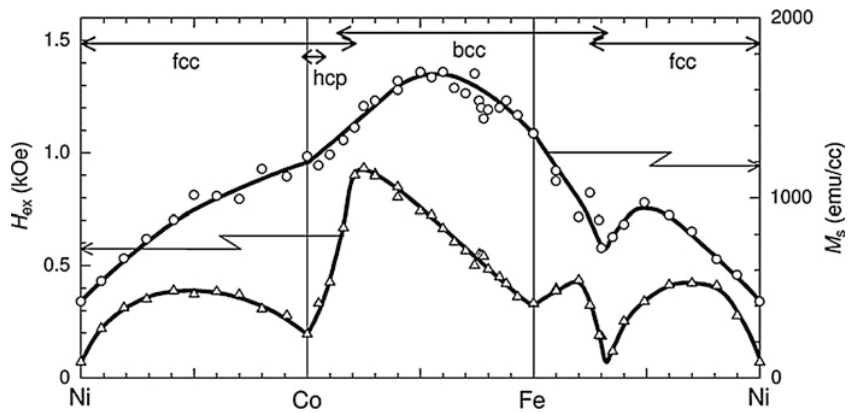


**Fig. 6** Exchange bias field, $H_{ex}$, and saturation magnetization, $M_S$, of Mn-Ir/FM (FM = Ni-Co, Co-Fe, Fe-Ni) bilayers as function of composition (© [2009] IEEE. Reprinted with permission from Ref. [36])

where pinning is irreversibly lost. Typical blocking temperature data for IrMn is shown in Fig. 5. The annealing temperature should be higher than the blocking temperature to properly induce exchange bias. While the annealing temperature is limited to ~300 ºC to avoid layer interdiffusion resulting in degradation of TMR characteristics and degradation of the shield magnetics, this limit is considerably higher than the blocking temperature. For IrMn, maximum exchange biasing is achieved for a layer thickness around 6–7 nm [33, 35] and in contact with a $CoFe_{25}$ pinned layer [36] as shown in Fig. 6. Other antiferromagnetic materials, for example, ~$Pt_{50}Mn_{50}$, also were used for spin and tunnel valves in the past. Compared to IrMn, however, PtMn only is antiferromagnetic in the chemically ordered $L1_0$ state. For this, ~12 nm PtMn needs to be deposited to induce chemical order during the annealing step. With shrinking read gap thickness, PtMn eventually was abandoned for IrMn due to its relatively large minimum thickness requirement.

Rather than using a single pinned layer as the reference layer, an antiparallel coupled pinned layer structure is commonly used [37, 38], which comprises the PL, typically a CoFe-based multilayer, being exchange coupled to the AF at its lower interface; the ACL; and the RL, typically a CoFe- and CoFeB-based multilayer, in contact with the tunnel junction at its upper interface.

The RL is antiferromagnetically coupled to the PL by the ACL via Ruderman-Kittel-Kasuya-Yosida (RKKY) interaction [39–41], so that the RL and PL magnetizations are oriented antiparallel to each other in low external magnetic fields. Since the RKKY coupling strength is oscillatory with ACL thickness due to quantum well effects originating from the band structure of the involved materials [42–44], the ACL needs to be deposited at a thickness yielding maximum antiferromagnetic coupling. Ru is commonly used as the ACL as it provides strong antiferromagnetic coupling for Co-based ferromagnets [45, 46]. Maximum antiferromagnetic coupling for Ru is achieved around 0.4 nm on the first and 0.8 nm thickness on the second peak depending on the CoFe composition of the PL and RL. Both PL and RL layers are designed to have about the same magnetization-thickness products, $M_{PL}t_{PL}$ and $M_{RL}t_{RL}$, respectively. As a result, flux closure between the two layers is achieved, and the net stray field on the free layer is minimized. Other advantages are that due to the low net moment, a high pinning field and enhanced thermal stability are achieved. The interfaces between the PL, ACL, and RL need to be very smooth, and the ACL needs to be pinhole-free. Both roughness [47] and pinholes [48, 49] induce biquadratic coupling, which needs to be avoided as it gives the RL the tendency to align orthogonal rather than antiparallel to the PL resulting in degraded magnetic stability of the sensor (for a review on biquadratic coupling mechanisms, see, e.g., Demokritov [50]).

DOI 10.1007/978-94-007-7604-3_35-1
© Springer Science+Business Media Dordrecht 2014

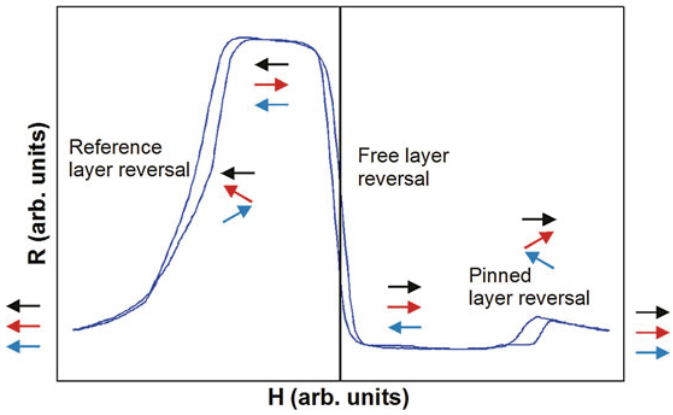


**Fig. 7** Resistance versus magnetic field and loop of a TMR sensor. *Arrows* indicate from top to bottom the free, reference, and pinned layer magnetization direction

Figure 7 shows a typical high field resistance versus applied magnetic field (R-H) loop of an antiparallel pinned read sensor. The arrows indicate from top to bottom the magnetization direction of the free, reference, and pinned layers. The field is applied along the pinned/reference layer direction. Thus, the free layer reversal is observed as a linear resistance change due to its stabilization by the hard bias in a direction orthogonal to the pinned and reference layers. At high fields, both the reference and pinned layers align in the direction of the field. As they reverse, they go into a spin-flop state, which is detectable as "bump" in the R-H loop. Modeling of hysteresis loops of antiferromagnetically pinned spin valves is shown by Beach et al. [51] and by Dimitrov et al. [52].

The MgO tunnel barrier is grown on top of the reference layer. The resistance of a TMR sensor is dominated by the RA product of the barrier which decreases as the barrier thickness is decreased. Generally, the RA product of a tunnel barrier drops exponentially as the thickness of the barrier is decreased; however, the RA product is also a function of materials and interface preparation. For tunnel junctions with areas of less than 100 nm × 100 nm (TW × SH), very thin barriers on the order of only a few angstroms are required to achieve resistance-area (RA) products ~1 $\Omega\mu m^2$ yielding a 100 Ω sensor, an impedance that is compatible with commercially available high-frequency amplifiers.

The growth of a very thin and smooth, pinhole-free tunnel barrier is key for good sensor performance and reliability. Atomic smoothness suppresses Néel interlayer coupling between the reference and free layers which contributes to signal nonlinearity and reduces possible signal levels. Pinholes in a tunnel barrier contribute to signal loss due to shunting, degrade magnetics due to magnetic pinhole coupling of the reference and free layers, and degrade reliability. However, as the physical dimensions (TW, SH) are further reduced with increasing recording densities, the RA product needs to be further decreased beyond the limitation of MgO. At the atomic layer thickness required for today's sensor, some imperfections such as pinholes cannot generally be prevented, and a decrease in TMR is observed. Thus, the search for alternative tunnel barrier materials with low RA products remains an area of extensive research. The free layer is deposited on top of the tunnel barrier. Similar to the other magnetic layers, the free layer is a multilayer to achieve required free layer properties. While it needs to be CoFe based to achieve high TMR, it also needs to exhibit soft magnetic properties, low magnetic damping for low magnetic noise, and low magnetostriction. NiFe or CoFeB among other materials helps to achieve these properties [53], and hence CoFe typically is multilayered with layers of CoFeB or NiFe.

DOI 10.1007/978-94-007-7604-3_35-1
© Springer Science+Business Media Dordrecht 2014

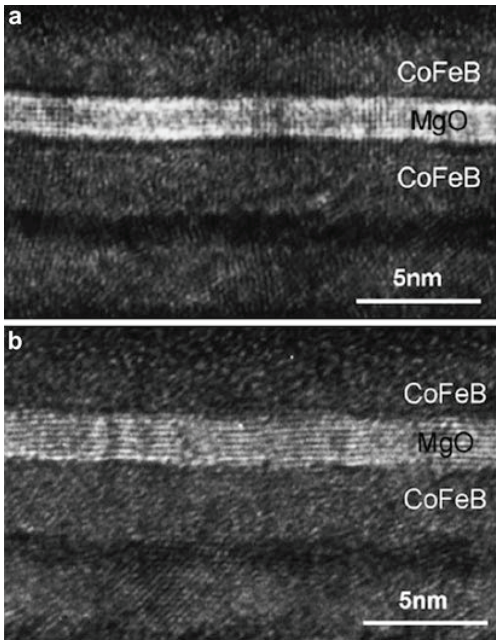


**Fig. 8** Typical high-resolution cross-sectional TEM image of (**a**) CoFeB/MgO(15 Å)/CoFeB tunnel junction and (**b**) CoFeB/Mg(4 Å)/MgO(15 Å)/CoFeB tunnel junction (Reprinted with permission from Ref. [54]. Copyright (2005), AIP Publishing LLC)

A high-resolution transmission electron microscopy (TEM) cross-sectional image of a typical low RA product of CoFeB/MgO/CoFeB tunnel junction is shown in Fig. 8 [54]. The TEM shows that the MgO is (100) textured and the crystalline quality very high, which leads to high TMR values.

Annealing of the tunnel junction stacks is not only needed to induce exchange bias, but it also increases TMR significantly due to improved interfaces and crystallinity of the electrodes [55]. However, annealing at too high temperatures degrades TMR due to interlayer diffusion. TEM and electron energy loss spectroscopy (EELS) studies revealed that depending on the preparation technique, various levels of $BO_x$ exist in the MgO barrier due to boron diffusion originating from the CoFeB layer after deposition [56, 57]. After annealing, the level of $BO_x$ is reduced while an interfacial layer of Mg-B-O layer is formed. While no interdiffusion of Co or Fe from the electrodes into the barrier is observed after annealing, the electrodes are mostly depleted of B (Fig. 9). The reduction of $BO_x$ levels in the tunnel barrier and the depletion of B in the electrodes are understood as the mechanism for improved TMR after annealing.

While Heusler alloys have been explored in epitaxial stacks as electrode materials for MgO-based tunnel junctions [17, 58], none of them are currently incorporated in read heads due to the requirement to process them at high temperatures to obtain chemical order and accordingly high spin polarization. Moreover, while high TMR can be achieved, other properties such as a sufficiently low interlayer coupling field and RA product are inferior to conventional CoFe(B)-/MgO-based tunnel junctions.

Apart from the magnetic layers described above, a set of seed and cap layers are needed. The seed layers are needed to facilitate the growth of the sensor stack and the antiferromagnet in particular with proper crystalline texture to provide for good magnetics and smooth interfaces. The use of magnetic seed layers which can act as part of the magnetic bottom shield is preferred in order to reduce the read gap. A nonmagnetic cap layer is deposited on top of the free magnetic layer to protect

DOI 10.1007/978-94-007-7604-3_35-1
© Springer Science+Business Media Dordrecht 2014

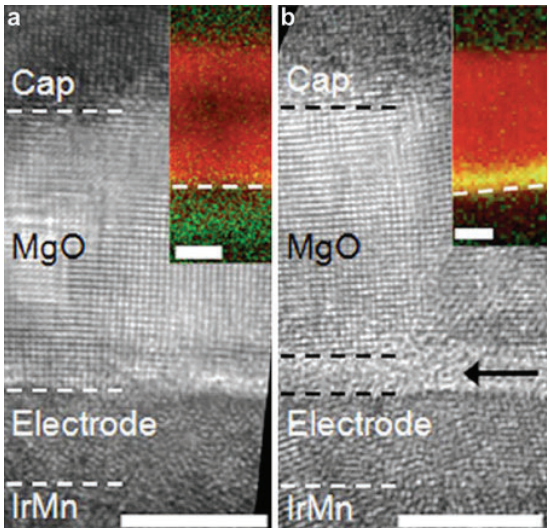


**Fig. 9** TEM images of a IrMn(15 nm)/CoFeB(4 nm)/MgO(10 nm)/cap film stack (**a**) before and (**b**) after annealing at 350 ºC (5 nm scale bar). An amorphous, interfacial layer forms after annealing as indicated by the *arrow* in (**b**). Insets (3 nm scale bar) show respective spectroscopic image of the stack before and after annealing in a red/green color scheme, where O and B are *red* and *green*, respectively. Mixing of *red* and *green* yields *yellow*, indicating the formation of an interfacial layer containing $BO_x$ (Reprinted with permission from Ref. [57]. Copyright (2009), AIP Publishing LLC)

the sensor from chemical and mechanical damages during processing. It also serves as a separation layer between the magnetic free layer and the magnetic top shield. The process above is described as a bottom-pinned structure with the antiferromagnetic layer and pinning structure below and the free layer above the tunnel barrier. In principle, it is possible to invert the stack with the antiferromagnetic layer and the pinned layer structure above and the free layer below the tunnel barrier. However, this top-pinned spin valve is not being used in any commercial TMR read sensor. The issues are generally lower exchange bias strength for a top-pinned structure compared to a bottom-pinned structure and the advantageous geometry of a bottom-pinned structure. In a bottom-pinned structure, the pinned layer structure typically has higher volume than the free layer due to the generally trapezoidal mill profile of the junction. Thus, pinned layer stability is gained due the larger volume of the pinned layer structure, and resolution is gained due to narrower width of the free layer.

CoPt or CoPtCr is typically used as hard magnetic material biasing the free layer. These materials have a hexagonal close packed (hcp) crystal structure. When deposited on body-centered cubic (bcc) seed layers such as Cr or Cr alloys [59], they will grow with their magnetic easy axis, the crystallographic c-axis, in the plane, so that the hard-bias magnetization is pointing at the free layer. The hard-bias field, which scales with the hard-bias remanent magnetization-thickness product (Mr*t), is penetrating the free layer and is stabilizing it in a direction perpendicular to the reference layer. The magnetization-thickness product of the free layer and the hard bias are adjusted so that the magnetic flux from the bits on the disk induces a free layer magnetization rotation within the designed utilization. A more detailed discussion about stability is given in the next section.

The total thickness of the insulator and hard bias with seed layers is restricted to the SSS; thus, the insulator and hard-bias seed layers can only be a couple of nm thick to allow for sufficient hard-bias material to be deposited to provide an adequate field for free layer stabilization. Within this thickness requirement, a hard-bias coercivity of around 2–3 kOe is typically achieved which warrants the stability of the hard bias against rotation or reversal in media fields. For historically large TW, the magnetization at the center of the free layer was mostly stabilized via magnetic exchange interaction

DOI 10.1007/978-94-007-7604-3_35-1
© Springer Science+Business Media Dordrecht 2014

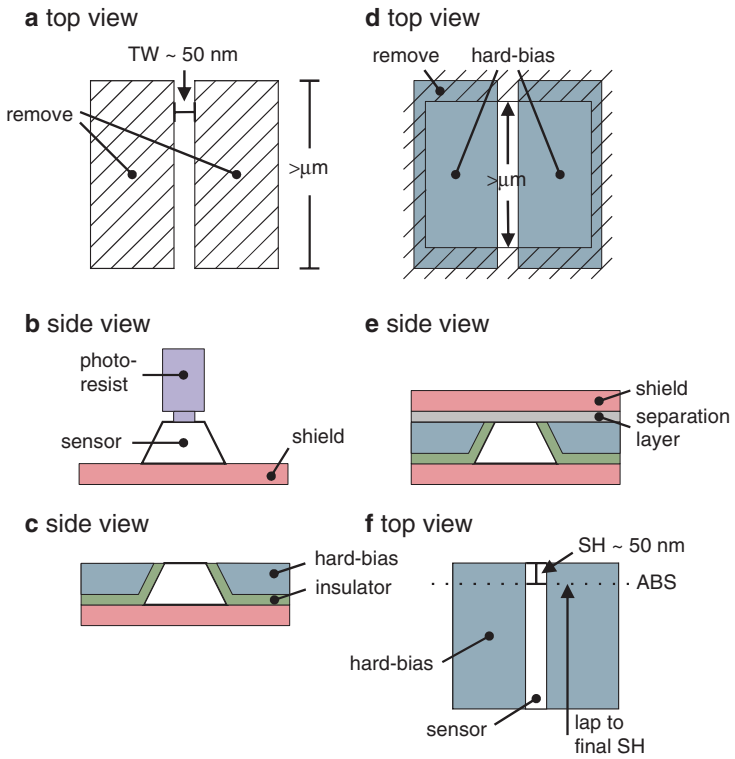


**Fig. 10** Not to scale views of (**a**) photo-pattern defining ~50 nm track width (*TW*), the hatched areas are removed by ion milling and refilled with insulator and hard bias. (**b**) Side view of photo-stencil on top of milled sensor on bottom shield. (**c**) Side view of sensor after milling and deposition of insulator and hard bias and subsequent lift-off step. (**d**) Top view of photo-pattern defining the initially several µm tall stripe height: the hatched area is removed by ion milling and is refilled with insulator, and the solid area corresponds to the refilled hard-bias area. (**e**) Side view of sensor with top shield and a separation layer magnetically isolating the hard bias from the top shield. (**f**) Top view of the sensor: the initially several µm tall stripe will eventually be lapped back to the ABS indicated by the *dotted line*, and the final stripe height (SH) is ~50 nm, similar to the TW

within the layer and thus rotated more than the magnetization at the edges. For today's small TW, the magnetization of the free layer is in a single-domain state and rotates in unison.

In the following, the processing steps of a simplified read-head manufacturing process are described. After the sensor stack is deposited on the wafer, first, the track width is defined by a first photolithographic step (Fig. 10a). After the photo-process, the material in the field is removed by ion beam milling (IBE) (Fig. 10b), and the sensor surfaces are then electrically insulated by ion beam deposition (IBD) or atomic layer deposition (ALD) of an insulator such as Al oxide. IBD offers high directionality, so that insulator material can be deposited even under the photo-stencil. ALD offers high-quality, highly conformal films due to layer-by-layer growth. However, ALD requires a wet chemistry at elevated temperature which can react with the side of the junction and may impact the sensor performance. After the insulator is deposited, the hard-bias structure with underlayers, the magnetically hard layer, and protective cap is deposited by IBD. The protective cap also serves as a magnetic separation layer between the hard bias and the top shield to prevent magnetic coupling of the hard bias and the shield and to minimize magnetic flux leakage from the hard bias into the shield and away from the free layer. Then the remaining photo-stencil and excess material are removed by a lift-off and planarization step (Fig. 10c), and the stripe height (SH) of the sensor is defined in a second photolithographic step (Fig. 10d). Again the material in the field is

DOI 10.1007/978-94-007-7604-3_35-1
© Springer Science+Business Media Dordrecht 2014

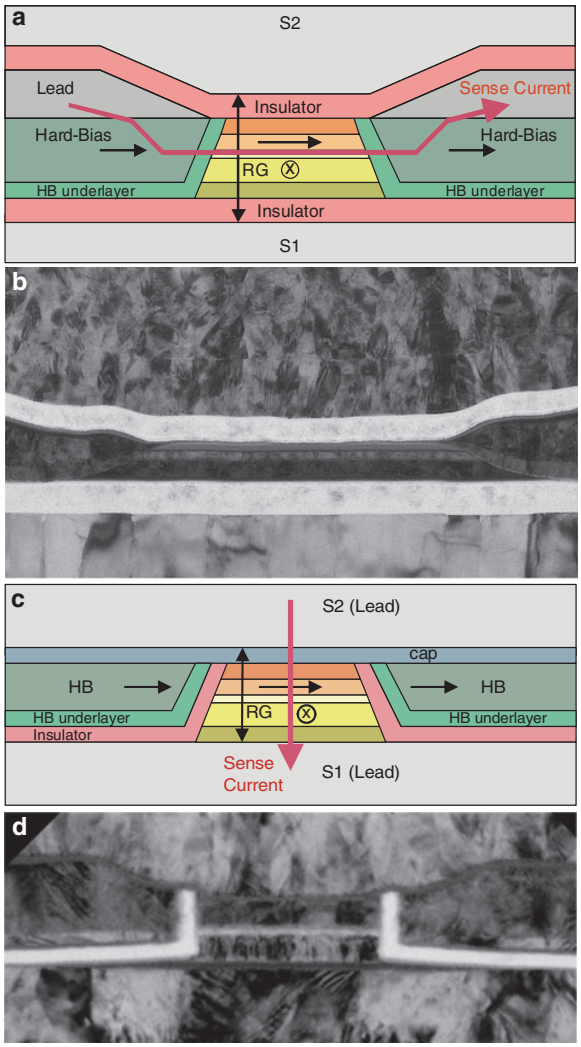


**Fig. 11** (**a**) Schematic view of a CIP-GMR sensor from the ABS. (**b**) TEM micrograph view of a CIP-GMR sensor from the ABS. (**c**) Schematic view of a CPP-TMR sensor from the ABS. (**d**) TEM micrograph view of a CPP-TMR sensor from the ABS

removed by IBE, and the structure is refilled by IBD or ALD with and insulator such as Al-oxide, and the remaining photo-stencil and excess material is removed by subsequent lift-off and planarization steps. The typical stripe height at this point of the process is several micrometers, so that the sensor is a long needlelike structure with a narrow TW and long SH. The structure is finally capped with a nonmagnetic separation layer, and the top shield (S2) is electroplated on top (Fig. 10e). After the write pole is formed on top of the reader (not shown), the wafer is eventually cut into smaller pieces called quads or mini-quads. These quads are diced into rows which comprise several recording heads. These rows are then lapped to the final stripe height of the sensor by mechanical polishing (Fig. 10f) and a protective carbon coating is deposited on the air-bearing surface. The final SH is of importance for magnetic sensor signal linearity and is typically of the same order as the TW.

DOI 10.1007/978-94-007-7604-3_35-1
© Springer Science+Business Media Dordrecht 2014

Because the sense current $I_S$ flows perpendicularly from the top shield S2 through the stack of layers to the bottom shield S1, the TMR read head is referred to as a current-perpendicular-to-the-plane (CPP) read head.

For comparison, Fig. 11a and c shows schematic cross-sectional views of a CIP-GMR and a CPP-TMR sensor, respectively, while Fig. 11c and d shows TEM micrographs of actual CIP-GMR and CPP-GMR recording heads, respectively. This particular view is the view an observer would have standing on the disk and looking up at the air-bearing surface of the recording head.

The TEM micrograph in Fig. 11d shows a photolithographically defined TMR reader junction with pinned and free layers separated by a tunnel barrier. The TEM also shows the hard-bias stabilization layers at either side of the junction separated from the junction by electrically insulating material and the bottom and top magnetic shields S1 and S2, respectively. From the figure, two critical dimensions of the head are visible which are the physical track width (TW) defined by the width of the junction and the magnetic read gap (RG) defined by the S1 to S2 spacing. Both of these dimensions are critical parameters defining performance. The magnetic read width (MRW) discussed further below is related to the TW.

Apart from the high signal in TMR, there also is a geometrical advantage of a CPP over a CIP sensor, such as the earlier generation CIP-GMR sensor. In a CIP sensor, the current enters the sensor through the hard bias which besides providing free layer stabilization also acts as lead structure. The antiferromagnet providing pinning and the cap provide a current shunt that is not contributing to the CIP-GMR signal. Moreover, the sensor and hard bias are electrically insulated from the bottom and top magnetic shields by layers of insulator, typically $Al_2O_3$. Thus, the physical read gap (RG), which is defined by the shield-to-shield spacing, is increased by the thickness of bottom and top insulators. In a CPP sensor, the magnetic shields act as the leads, and thus no bottom and top insulators which add to the RG are required. The sensor is grown directly onto the bottom shield, and only a thin metallic cap is needed to separate the hard bias and the top shield from interacting magnetically. In contrast to a CIP sensor, no current is shunted by any of the layers but rather flows through the sensor. The antiferromagnet and the caps only add a small series resistance compared to the tunnel barrier resistance.

Since the formation of a CPP junction for TMR heads is very time consuming and expensive, a much simpler method to test film level TMR quality for film development and manufacturing process control purposes is used. For this, a series of four-point probe measurements on TMR films with varying probe spacing is conducted with typical probe spacing being in the μm range. As the probe spacing is varied, a nonlinear change in R and a peak in MR is observed. By fitting the curves, a prediction about film TMR and RA values can be made [60]. In practice, an array of probes on cantilevers is used; instead of physically varying the probe spacing, four probes of the array with desired spacing are selected and engaged simultaneously at a time. However, since the peak in MR shifts to narrower probe spacing for films with lower RA values, it is difficult to make good predictions for films with low RA values with commercially available probe arrays. While it is simple to characterize junction with RA values well above 1 $\Omega$-$\mu m^2$, it has become challenging to characterize junctions of interest that have RA values well below 1 $\Omega$-$\mu m^2$. For this, ultrafine probes are required, which by themselves are challenging and expensive to manufacture.

## Magnetic Read-Head Design

Generally, the TMR effect follows the simple geometrical relationship

DOI 10.1007/978-94-007-7604-3_35-1
© Springer Science+Business Media Dordrecht 2014

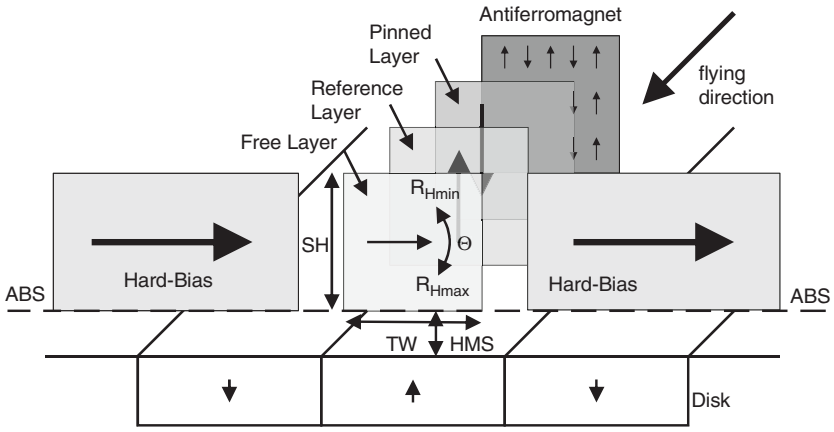


**Fig. 12** Schematic view of a TMR magnetic recording head. The free layer is stabilized by the hard bias in a direction parallel to the air-bearing surface (*ABS*) of the head, while the pinned and reference layers are stabilized by an antiferromagnet via exchange bias perpendicular to the ABS. The ABS is indicated by a *dashed line*

$$\mathrm{TMR} = \left(\frac{R_{AP} - R_P}{R_P}\right)_0 \cos\left(M_1, M_2\right) \tag{2}$$

where $R_{AP}$ and $R_P$ are the resistance values of the TMR stack in the configuration of antiparallel and parallel alignment of the magnetizations ($M_1$ and $M_2$) of the two ferromagnetic layers adjacent to the tunnel barrier, respectively. The TMR varies with the cosine of the angles between the two magnetizations. In a TMR structure such as read head or an MRAM cell, these layers are generally referred to as the free and reference layers. However, unlike in an MRAM cell where full reversal of the free layer magnetization from parallel to antiparallel alignment with respect to the reference layer and a finite switching field is desired to maximize TMR and stabilize the bit, a read sensor is a linear analog device, and thus only small rotations of the free layer magnetization are utilized.

A schematic view of a TMR read-sensor comprising a free layer, the tunnel barrier, reference layer, pinned layer, and antiferromagnet all flying at some head-media spacing (HMS) above a recorded media is shown in Fig. 12. The lateral dimension of the free layer is called the track width (TW), and the height of the free layer, the stripe height (SH). In order to linearize the response of a TMR read sensor, the free and reference layer magnetizations are prepared perpendicular to each other in the quiescent state in which no field is applied. While the directionality of the reference layer magnetization is pinned perpendicular to the air-bearing surface (ABS) of the sensor by being exchange coupled to an antiferromagnet, the directionality of the free layer is established parallel to the ABS by the magnetic field of the hard-bias deposited on each side. A rotation of the free layer magnetization will lead to the variation of the angle between the magnetization directions of the reference and free layers, which is detectable as the change in electrical resistance.

For small angle excitations Θ of the free layer magnetization by external fields, a linear response is achieved. This can easily be understood as the first-order approximation of the cosine in Eq. 2 by a power series at 90° simply is a linear function. The resistance-field (R-H) curve resulting from the field excitation is referred to as a transfer curve. Examples of a properly stabilized (and hence linearized) and a non-stabilized (and hence non-linearized) transfer curve are shown in Fig. 13.

A side view of the sensor is shown in Fig. 14. The sensor is located between the top and bottom shields, which define the read gap. The shields serve the purpose of shielding the flux from adjacent bits outside the read gap so that only the magnetic bits within the gap are read by the sensor. Signal

DOI 10.1007/978-94-007-7604-3_35-1
© Springer Science+Business Media Dordrecht 2014

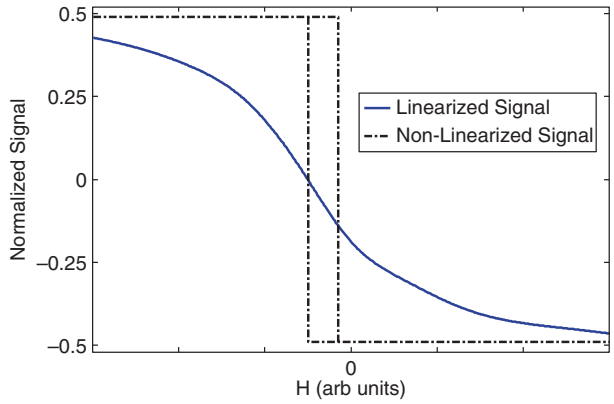


**Fig. 13** Linearized and non-linearized transfer curves. The nonlinear transfer curve exhibits hysteretic switching from an antiparallel to a parallel state, and the linearized transfer curve does not exhibit any hysteresis

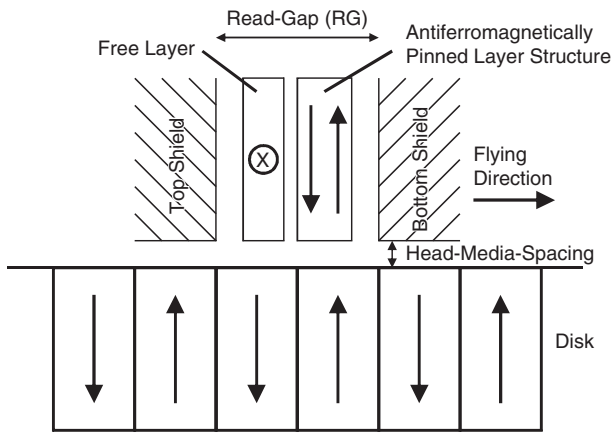


**Fig. 14** Read head located between bottom and top shields. The read gap is typically on the order of two recorded bits

detection methods extract the signal of interest even with interference from adjacent bits, so typically about two bits can be located under the sensor and still resolve the signal from each bit.

The linear density, a measure how densely bits can be packed on a recorded track, is determined by the pulse width parameter, $PW_{50}$, which is given by [61]

$$PW_{50} = \sqrt{RG^2 + 4(HMS + a)^2} \tag{3}$$

where *RG* is the read gap defined by the shield-to-shield spacing (adjusted for any magnetic seed layer thickness), *HMS* is the head-media spacing, and *a* is the media transition length. The HMS is given by the thickness of the media overcoat (not shown), the fly height of the read head over the medium, and the head overcoat (not shown). Lower read gap, head-media spacing, and transition length all lead to higher linear density.

As the fly height was reduced from several μm to just a couple of nm as areal density was increased over the years, it also became necessary to control it more actively. For this, a resistive heating element is now implemented in any recording head for thermal fly-height control (TFC) [62]. The ABS profile and the flying characteristics are modified by the thermal protrusion when the

DOI 10.1007/978-94-007-7604-3_35-1
© Springer Science+Business Media Dordrecht 2014

TFC resistive heater is activated. Tuning of the ABS protrusion with the TFC power allows tuning of the fly height. The introduction of TFC resistive heaters reduced variations in fly height and allowed the head to fly closer to the disk, enabling further dimensional scaling while minimizing head disk interactions and maintaining low bit error rates.

In a recording head, the energy density of the free layer can be described by a single-domain free energy model

$$E = K_U t_{FL} \cos^2\Theta - H_{ext} M_S t_{FL} \cos\Theta - J_{\text{int}} \cos\Theta - H_{HB} M_S t_{FL} \sin\Theta \tag{4}$$

where the first term is an uniaxial anisotropy term, $K_U$ is the anisotropy constant and $t_{FL}$ the free layer thickness, the second term is the Zeeman energy, $H_{ext}$ is the externally applied magnetic field and $M_S$ is the free layer saturation magnetization, the third term is the interlayer coupling energy between the free and reference layers with coupling constant $J_{\text{int}}$, and the fourth term is the hard-bias effective field with field $H_{HB}$. The reference layer direction is assumed to be spatially fixed perpendicular to the ABS and parallel (or antiparallel) to the external field $H_{ext}$. $\Theta$ is the angle between the reference layer magnetization direction and the free layer magnetization direction. The uniaxial anisotropy term $K_U$ comprises the shape anisotropy $K_S$ (TW, SH), magnetocrystalline anisotropy, and magnetoelastic anisotropy energy $K_\sigma = 3/2\ \lambda\sigma$ with the magnetostriction coefficient $\lambda$ and the intrinsic stress $\sigma$. The shape anisotropy is positive if TW > SH and negative if TW < SH. The stress in the TMR stack usually is compressive ($\sigma < 0$). Thus, $K_U$ is positive (negative) when the free layer exhibits negative (positive) magnetostriction. Negative magnetostriction is preferred to stabilize the free layer in the direction parallel to the ABS. Minimization of the energy with respect to $\Theta$ yields the relationship

$$h = m - j_{\text{int}} + h_{HB} \frac{m}{\sqrt{1 - m^2}} \tag{5}$$

where $h = \frac{H_{\text{ext}}}{H_K}$, $h_{HB} = \frac{H_{HB}}{H_K}$, and $j_{\text{int}} = \frac{J_{\text{int}}}{2K_U t_{FL}}$ are the normalized external field, hard-bias field, and interlayer coupling field, respectively, $H_K = \frac{2K_U}{M_S}$ is the anisotropy field, and $m = \cos\Theta$ is the free layer magnetization component along the reference layer axis. The resulting resistance-field (R-H) curve in normalized units is shown in Fig. 15.

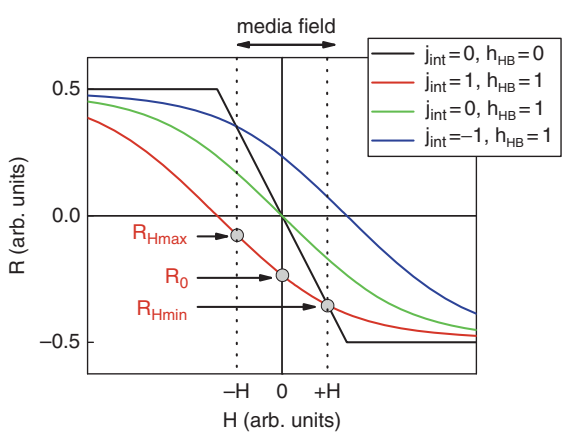


**Fig. 15** Transfer curves: An increased interlayer coupling field leads to an asymmetry and bias point shift. An increased hard-bias field leads to a higher saturation field

DOI 10.1007/978-94-007-7604-3_35-1
© Springer Science+Business Media Dordrecht 2014

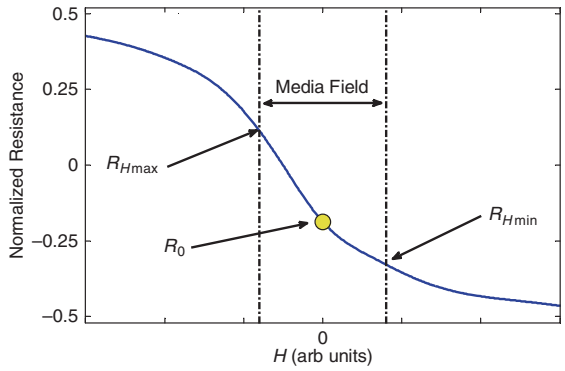


**Fig. 16** Utilization is defined as the portion of the R-H curve that is used for magnetic read back, where $R_{H\max}$ and $R_{H\min}$ are the sensor resistances for negative and positive fields from the media

The saturation field increases with hard bias; accordingly, the R versus H slope decreases. Depending on the sign of the interlayer coupling field, a lower or higher bias point (*BP*) and positive or negative asymmetry (A) are observed. The *BP*, ranging from 0 to 1, represents the angle of the FL with respect to the reference layer at zero field (H = 0)

$$BP = \frac{R_0 - R_P}{R_{AP} - R_P} \tag{6}$$

where $R_0$ is the resistance at $H = 0$ and $R_{AP}$ and $R_P$ are the sensor resistances when the free and reference layers are antiparallel and parallel, respectively

$$A = \frac{|R_{H\max} - R_0| - |R_0 - R_{H\min}|}{|R_{H\max} - R_0| + |R_0 - R_{H\min}|} \tag{7}$$

where $R_{H\max}$ and $R_{H\min}$ are the maximum and minimum sensor resistances measured at full media excitation as shown in Figs. 12, 15, and 16

For a linear response during the read-back process, the FL angle at $H = 0$ should be close to parallel to the ABS and orthogonal to the reference layer. However, as conveyed by the simple calculation above, several factors such as the magnetic field from the hard bias, the shape anisotropy, the magnetostriction, the crystalline anisotropy, and the interlayer coupling determine the actual bias point. A positive coupling field results in positive asymmetry and lower bias point, while negative coupling field results in negative asymmetry and higher bias point. The magnetic coupling field in a TMR head generally is positive due to roughness-induced Néel coupling [63, 64]; thus, positive asymmetry and lower BP are observed. An experimental transfer curve is shown in Fig. 16.

As mentioned above, only a small portion of the transfer curve is utilized to obtain a linear read-back signal. The sensor utilization, u, is given by the ratio of the resistance change of the sensor while reading back the recorded bits on the media and the resistance change between antiparallel and parallel orientations of the free and reference layers. It is proportional to the rotation of the free magnetization as it is interacting with the magnetic field from the recorded bits and is expressed as

$$u = \frac{R_{H\max} - R_{H\min}}{R_{AP} - R_P} \propto \cos\left(\Theta_{FL\max} - \Theta_{RL}\right) - \cos\left(\Theta_{FL\min} - \Theta_{RL}\right) \tag{8}$$

DOI 10.1007/978-94-007-7604-3_35-1
© Springer Science+Business Media Dordrecht 2014

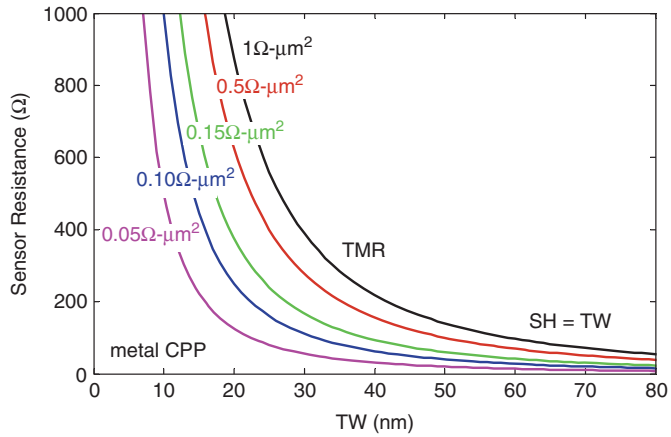


**Fig. 17** Sensor resistance as function of TW for various RA products (assuming TW = SH)

where $\Theta_{FL\max}$ and $\Theta_{FL\min}$ are the angles of the free layer corresponding to $R_{H\max}$ and $R_{H\min}$, respectively. Here, like usual, it is assumed that the angle of the reference layer $\Theta_{\mathrm{RL}}$ does not change direction during read-back operation due to a sufficiently large pinning field exceeding the media field. The utilization of the device will depend on the magnetic field from the hard-bias field penetrating the free layer, or the stripe height and the track width of the sensor, among other factors. The utilization will decrease with decreasing stripe height or increasing track width due to demagnetization fields and with hard-bias field strength. The higher the utilization, the higher the measured signal, however at the expense of added nonlinearity in signal. To maintain linear read-back signals, typical utilization factors u are below 0.5. The read-back signal is given by

$$\text{Signal} = V_b \frac{R_{AP} - R_P}{R_0} u = V_b \frac{R_{\max} - R_{\min}}{R_0} \tag{9}$$

where $V_b$ is the bias voltage across the sensor.

As areal densities continue to increase through reduction of the physical geometries, the sensor RA product needs to decrease accordingly to obtain reasonable device impedance. The device impedance range is constrained by the target data rate, the system noise requirements, and the compatibility with the commercially available amplifiers. The resistance of a TMR read head, in the absence of an external field, is determined by a combination of the TW, SH, RA product, TMR ratio, and bias point (BP):

$$R = RA \frac{1 + BP * TMR}{TW * SH} \tag{10}$$

Typically, the sensor resistance ranges from 100 to 1,000 Ω. To maintain this nominal resistance range, the sensor RA product needs to decrease as 1/(TW*SH) with increased areal density. Without properly scaling the RA-product, then too high of a device resistance will result in two primary performance penalties. First, high resistance can attenuate the read-back signal at higher data rates from the RC roll-off. Second, high resistance results in increased Johnson and shot noise from the TMR element and higher current noise from the high-bandwidth amplifier.

DOI 10.1007/978-94-007-7604-3_35-1
© Springer Science+Business Media Dordrecht 2014

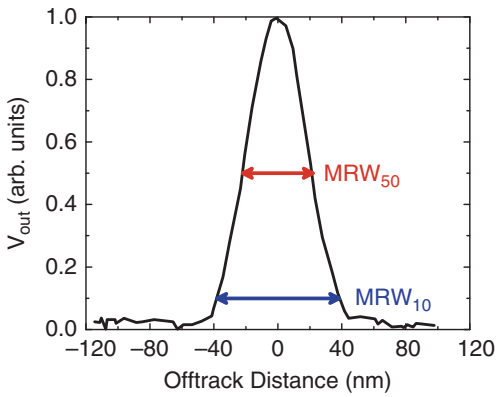


**Fig. 18** Typical microtrack profile showing the measured signal as a function of offtrack position. $MRW_{50}$ is a measure of track width, and $MRW_{10}$ is a measure of sensitivity to adjacent tracks

The scaling of sensor resistance R with TW (assuming TW = SH) is shown in Fig. 17. The typical RA range for TMR sensors from 0.5 to 1 Ω-μm$^2$ and for CPP-GMR sensors from 0.05 to 0.1 Ω-μm$^2$ is indicated.

With the growth in areal density and the progress in deposition and process technology, read heads utilizing MgO tunnel junctions have continued to scale in RA product, which now is well below 1 Ω-μm$^2$, while maintaining high TMR ratios. Thus, although always presumed to be close to the end of life, the era of TMR sensors may continue for several years to come.

While the physical track width (TW), shown in Fig. 12, is lithographically defined, the read-head response to the recorded tracks on the media determines the magnetic read width (MRW). This magnetic read width is a key factor determining the physical written track spacing (or track pitch) and therefore one of the two key components determining the areal density, the other being linear density. One may expect the MRW will be related to the physical TW and more specifically to the physical width of the free layer. The magnetic width is typically larger than the physical width due to the recorded tracks not being directly below the sensor. As HMS increases, the sensor will respond to fields further away from the physical track, resulting in a larger MRW for the same physical TW. The standard method to determine the MRW involves measuring the cross-track signal on a narrow written track width, commonly referred to as a microtrack. The microtrack can be prepared by writing an isolated track of interest over some background tracks [65]. The track of interest is then narrowed by AC erasing portions of the track from the edge. Ideally, the microtrack should be as narrow as possible, but certainly narrower than the MRW of the reader, to accurately determine MRW. Additional tracks are prepared at some distance away to assess sensitivity to adjacent tracks. Once the microtrack is prepared, the read-head signal is measured as the head is scanned in the cross-track direction over the microtrack. The resulting signal versus offtrack position (OTP) generates a microtrack profile. The MRW is defined as the full width at half maximum of this microtrack profile, or the distance where the signal has decreased to 50 % of the peak signal ($MRW_{50}$). Additionally, the sensitivity to adjacent tracks is characterized by the width where the signal has decreased to 10 % of the peak signal ($MRW_{10}$). The ratio of the $MRW_{50}/MRW_{10}$ determines, in part, the reader performance as the head is moved off the center of any written track.

Scaling the MRW, and therefore the physical track width, is crucial for scaling the areal density. The physical stripe height (SH) of the sensor is not as closely related to the areal density as the physical TW of the sensor; rather, the optimal SH is determined by sensor stability as discussed above. To maintain a linear response signal, the SH is adjusted to obtain a well-stabilized FL

DOI 10.1007/978-94-007-7604-3_35-1
© Springer Science+Business Media Dordrecht 2014

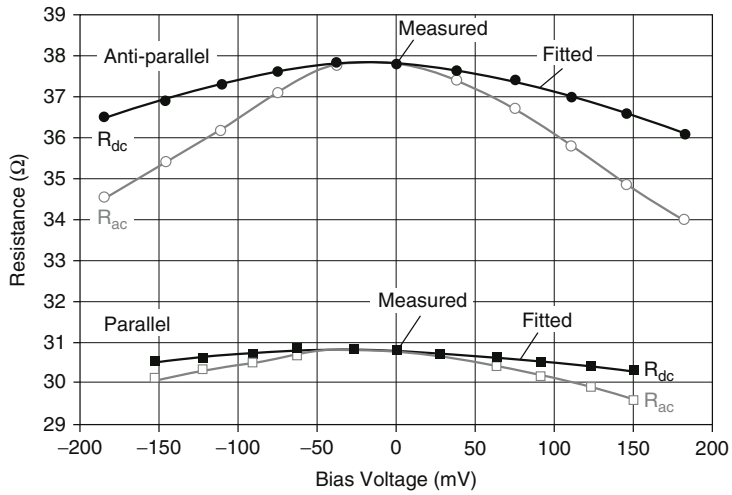


**Fig. 19** Measured $R_{AC}$ and $R_{DC}$ with increasing bias voltage (© [2004] IEEE. Reprinted with permission from Ref. [69])

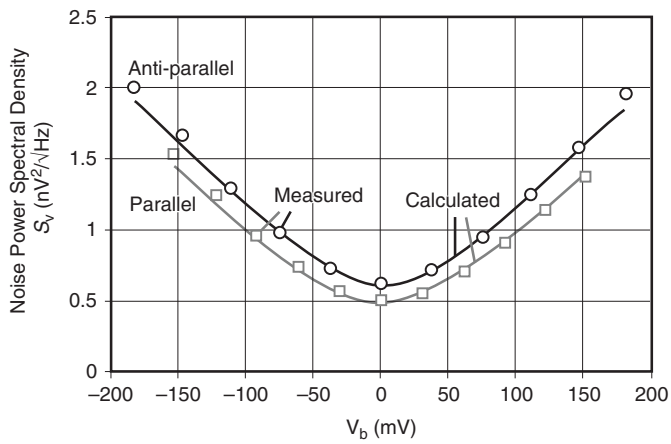


**Fig. 20** Calculated (after Eq. 11) and measured noise power density curves with bias voltage for a tunnel junction in the parallel and antiparallel states. The noise is higher in the antiparallel state due to higher resistance (© [2004] IEEE. Reprinted with permission from Ref. [69])

exhibiting coherent magnetization rotation. Generally, this is achieved with a TW/SH aspect ratio near 1. A tall SH enhances pinned layer stability but tends to destabilize the free layer.

Another issue going forward will be that as sensor dimensions are reduced, the number of crystalline grains in the sensor layers and the hard-bias layers is reduced, giving rise to statistical variations in the strength and angle of the pinning and hard bias and increased noise [66].

## SNR Requirements of a Magnetic Recording Head

Adequate signal-to-noise ratio from the read head is required to provide acceptable drive performance. The signal is determined by the bias voltage, the magnetoresistance ratio, and the utilization

DOI 10.1007/978-94-007-7604-3_35-1
© Springer Science+Business Media Dordrecht 2014

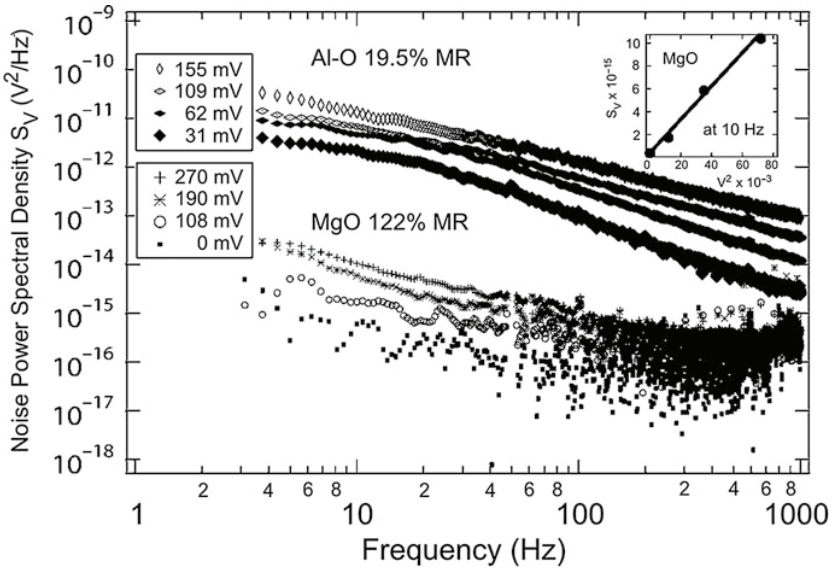


**Fig. 21** Noise power spectral density $S_V$ as a function of frequency of Al-Ox and MgO tunnel junctions at different bias voltages in parallel magnetization state. Inset, $S_V$ measured at 10 Hz frequency as a function of bias field for the MgO junction (Reprinted with permission from Ref. [73]. Copyright (2006), AIP Publishing LLC)

factor; however, multiple noise sources are present to influence the SNR. The noise components in a TMR sensor are Johnson/shot noise, magnetic noise, frequency-dependent noise such as 1/f, RTN, or spin-torque noise (for a review, see Lei et al. [67]).

Shot noise originates from fluctuations of electrons tunneling through the barrier when a bias is applied across the sensor. Generally, it is assumed that these fluctuations are obeying a Poisson distribution, in which case the noise power can be written as [68, 69]

$$S = 2eV_b \frac{R_{AC}^2}{R_{DC}} \coth(qV_b/2\mathrm{k_B}T) \tag{11}$$

where e is the charge of the electron, $V_b$ is the voltage applied across the barrier, $\mathrm{k_B}$ is the Boltzmann constant, $T$ is the absolute temperature, $R_{AC} = dV/dI$ is the differential resistance across the barrier at bias voltage $V_b$, and $R_{DC} = V_b/I_b$ is the DC sensor resistance. $R_{AC}$ and $R_{DC}$ decrease both in the parallel and antiparallel states with increasing bias voltage as the barrier height is lowered for tunneling electrons as shown in Fig. 20. The corresponding noise spectrum is shown in Fig. 21.

In the shot noise regime of high bias voltage $V_b >> \mathrm{k_B}T$, the noise power is given by $S_S = 2qI_BR_{AC}^2$ and increases with bias current; in the Johnson noise regime of low bias voltage $V_b << \mathrm{k_B}T$, the noise is given by $S_T = 4R_{DC}\mathrm{k_B}T$, where it behaves like thermal white noise given by the Nyquist equation which is simply proportional to device resistance and temperature.

TMR sensors exhibit frequency-dependent noise of magnetic and nonmagnetic origins. The magnetic contribution is associated with magnetization fluctuations in the free, pinned, or reference layers. The nonmagnetic electronic contribution is associated fluctuations in conductivity due to defects or impurities in the tunnel barrier allowing for pinhole conduction via charge trapping and detrapping.

$1/f$ noise, which is noticeable as excess low-frequency noise, is an important contributor to the total noise power of a TMR sensor. $1/f$ noise is commonly observed in other electronic components such as semiconductor diodes and transistors, but it is interesting to note that this type of noise is not

DOI 10.1007/978-94-007-7604-3_35-1
© Springer Science+Business Media Dordrecht 2014

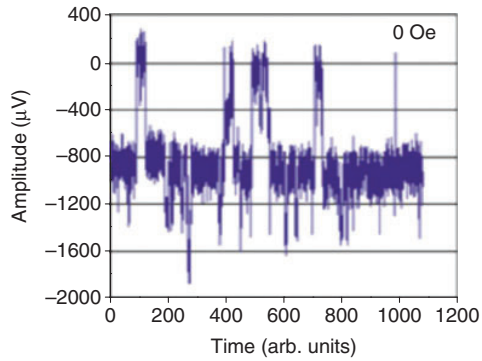


**Fig. 22** RTN trace showing fluctuations between two different metastable resistance levels (Reprinted with permission from Ref. [76]. Copyright (2009), AIP Publishing LLC)

only limited to electronic devices but is also observed in biological, chemical, geological, or economic systems. The underlying reasons for 1/*f* noise can be plentiful, but most importantly, the apparently random fluctuation of a given parameter in the system under consideration is extrinsic and will depend on the history of prior fluctuations.

The noise power scales like

$$S_{1/f} = S_0 \left(\frac{f_0}{f}\right)^{\eta} \tag{12}$$

where the exponent η is determined by the underlying mechanism of the noise. While $\alpha = 1$ gives the classical 1/*f* noise, other exponents $0 < \eta < 2$ are possible [70].

Christensson et al. [71] showed how a 1/*f* spectrum in MOS transistors with electron traps in the oxide is achieved if decay rates scale exponentially with distance of the traps from the silicon/oxide interface.

A 1/f noise spectrum for a magnetic tunnel junction is shown in Fig. 21 [72]. There the 1/f noise is of electronic origin as it is dependent on the bias voltage. Since $(1/f)^{\eta}$ noise originates from structural or magnetic defects, it often can be reduced by extensive annealing [73].

Closely related to 1/*f*-type noise is random telegraph noise (RTN), where fluctuations between two – sometimes even more – discrete states are observed with time (Fig. 22). For constant decay rates of each state, the spectrum rolls off in a $(1/f)^2$ fashion [74]. RTN noise is commonly observed in TMR devices [75, 76] and is given by

$$S_{\mathrm{RTN}} = \frac{S_0}{1 + (f/f_0)^2} \tag{13}$$

Thermal fluctuations of the magnetic layers, referred to as mag-noise, is yet another frequency dependent noise source. Mostly mag-noise is observed in the free layer but can be observed in the reference and pinned layers as well. Typically at frequencies below 1 GHz, the mag-noise is "white" or frequency independent [77], but exhibits a ferromagnetic resonance peak at higher frequency [78, 79]. Mag-noise fluctuations in a magnetic layer are proportional to the signal and inversely proportional to the volume of the magnetic layers:

DOI 10.1007/978-94-007-7604-3_35-1
© Springer Science+Business Media Dordrecht 2014

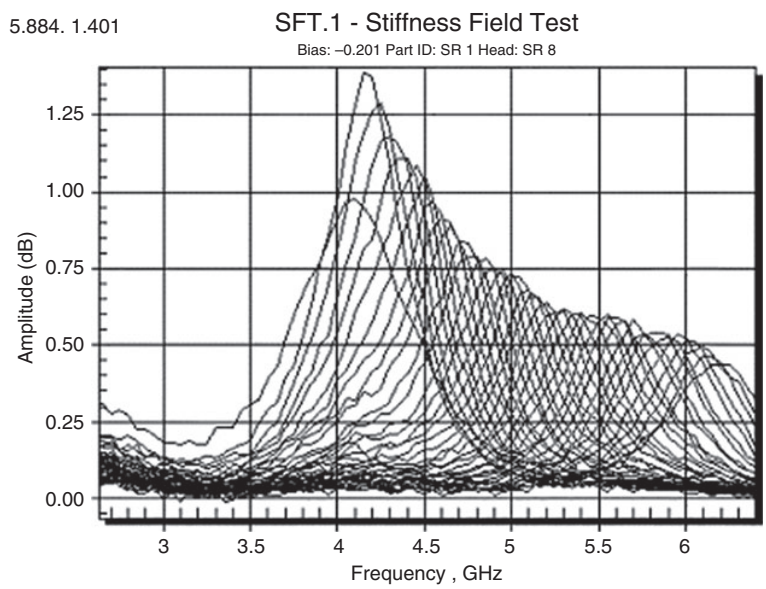


**Fig. 23** FMR spectra of a TMR sensor captured during a longitudinal field sweep from 300 Oe (4.1 GHz) to 800 Oe (6.2 GHz) (© [2009] IEEE. Reprinted with permission from Ref. [81])

$$S_M = (I\Delta R)^2 \frac{4gk_B T\alpha}{M_F V_F} \frac{g^2 H_\perp^2 + \omega^2}{\left(\omega^2 - \omega_0^2\right)^2 + (\omega\Delta\omega)^2} \tag{14}$$

where $M_F$ is the magnetic layer saturation magnetization, $V_F$ is the volume of the magnetic layer, $H_\perp$ is the out-of-plane stiffness field, $g$ is the gyromagnetic ratio, $k_B$ is the Boltzmann constant, $T$ is the absolute temperature, and $\alpha$ is the magnetic Gilbert damping constant. A more general form of is given by Smith and Arnett [78]. The ferromagnetic resonance (FMR) frequency $\omega = g\sqrt{H_\perp H_{||}}$ is in the GHz range, and the linewidth $\Delta\omega = g\alpha(H_\perp + H_{||})$ increases with in-plane ($H_{||}$) and out-of-plane ($H_\perp$) stiffness fields. Assuming that the free layer is stabilized by the hard-bias field $H_{HB}$, the in-plane stiffness field is $H_{||} = 2H_{HB}$; the out-of-plane stiffness field is $H_\perp = H_D - H_{K\perp}$, where $H_D$ is the demagnetization field; and $H_{K\perp}$ is the out-of-plane anisotropy field. Higher stiffness fields, which lead to a higher FMR frequency, lower the noise but also lower the sensitivity due to lower utilization. Conversely, lower stiffness fields, which lead to a lower FMR frequency, increase the noise, but increase the sensitivity due to higher utilization. Thus, FMR measurements can be a good indication for noise and sensitivity. The FMR spectra of a TMR sensor as the longitudinal magnetic field is swept from 300 Oe to 600 Oe are shown in Fig. 23 [80]. Both the FMR frequency and linewidth increase as the magnetic field is increased.

At higher areal densities and smaller physical geometries, the mag-noise is a dominating source of reader noise. In this regime, higher signal from improved TMR, higher bias voltage, and larger utilization factors will generate equally higher noise and hence provide no overall SNR improvement. Options for reducing the mag-noise rely on lowering the Gilbert damping parameter $\alpha$ or increasing the magnetic volume of either the free layer or reference layer while maintaining the required TW and shield-to-shield spacing.

Another frequency dependent source of noise are spin-torque induced fluctuations of the free or reference layers. Spin torque is a phenomenon that originates from the interaction of spin-polarized electrons flowing through a magnetic layer and interacting with its magnetic moment, thereby

DOI 10.1007/978-94-007-7604-3_35-1
© Springer Science+Business Media Dordrecht 2014

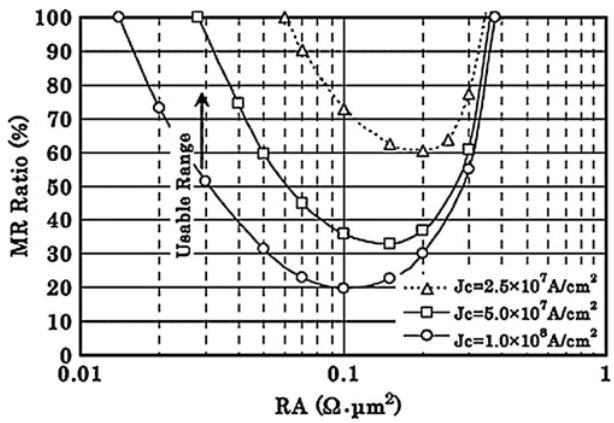


**Fig. 24** Usable range of MR ratio and RA at 2 Tb/in$^2$. The usable ranges are the upper side of each Jc line. Jc is the critical current density due to spin-transfer torque (© [2010] IEEE. Reprinted with permission from Ref. [91])

exerting a torque that aligns the magnetization direction with the polarization of the electrons. The effect was theoretically independently postulated in 1996 by Berger [81] and Slonczewski [82]. After the first experimental verification [83, 84], the topic became an area of intense research for its application to spin-electronic devices. In respect to a magnetic recording sensor, however, spin torque is observed as noise [85]. Spin-polarized electrons flowing from the reference to the free layer will destabilize the free layer when it is aligned antiparallel to the reference layer, while spin-polarized electrons flowing from the free to the reference layer reflected at the reference layer destabilize the free layer when it is aligned parallel to the reference layer (for a review on the topic of spin-torque excitations in magnetic devices, see Katine and Fullerton [86]). The critical current density for spin-torque-induced instabilities on the free layer magnetization direction is [86–89]

$$j_{\text{crit}} = \frac{4\pi e}{h}\frac{\alpha M_F t_F}{P}\frac{\left(H_{\|} + H_{\perp}\right)}{(1-q^2)d\beta(q)/dq - 2q\beta(q)} \tag{15}$$

where $q = \cos\varphi$ is the cosine of the angles between free and reference layers; $\alpha$ is the Gilbert magnetic damping coefficient; $P$ is the net spin polarization of the current inside the spacer layer; $\beta(q)$ is the Slonczewski coefficient describing the angular dependence of the spin-transfer torque; $M_F$ and $t_F$ are the free layer magnetization and thickness, respectively; $e$ is the electron charge; h is the Planck constant; and $H_{\perp}$ and $H_{\|}$ are the same out-of-plane and in-plane stiffness fields as defined above. The general form of the Slonczewski coefficient $\beta(q)$ is given, for example, by Xiao et al. [90] and depends on the material system under consideration. For TMR sensors, β assumes a symmetric form in $q$, while for CPP-GMR sensors, it is asymmetric in $q$. The asymmetry in a CPP-GMR structure is founded in the multiple reflections the electrons undergo at the free layer/spacer and spacer/reference layer interfaces. Due to the long spin-diffusion length of the spacer layer and the sensor structures being generally nonsymmetric, the spacer layer may become polarized in a direction which is not the arithmetic mean between the free and reference layer magnetizations. Accordingly, for a CPP-GMR sensor where electrons are flowing from the free to the reference layer, an operation with the free and reference layers in a more parallel state is preferred for stability. It is important to note that the spin-torque critical current density increases with magnetic damping and thus spin-torque noise is reduced with magnetic damping. However, thermal magnetic noise is increased with damping. Moreover, the spin-torque critical current density decreases with spin

DOI 10.1007/978-94-007-7604-3_35-1
© Springer Science+Business Media Dordrecht 2014

polarization, and thus, while high spin polarization is desirable to obtain high TMR or CPP-GMR, it will also increase the susceptibility to spin-torque noise.

Due to the fairly high RA product of ~1 Ω-μm$^2$ in TMR sensors, current densities are small and spin-torque noise is not a limiting factor. Thus, it is desirable to implement free layers with low magnetic damping to reduce thermal magnetic noise and high spin-polarization alloys to increase signal. For CPP-GMR sensors however, which are discussed further below, spin-torque-induced noise is a major impediment. There RA values are typically ~50 m Ω-μm$^2$, and accordingly, the critical current density for the onset of spin-torque excitations often is lower than the required sense current density. To reduce spin-torque noise in a CPP-GMR, it is desirable to implement free layers with high magnetic damping. To obtain high signal for CPP-GMR devices, highly spin-polarized alloys like Heusler alloys are considered. These however exhibit low magnetic damping due to their high spin polarization giving rise to spin-torque instabilities. This obviously imposes a dilemma.

One of the most important metrics to assess reader performance is reader signal-to-noise ratio (SNR). The others are being resolution and reliability. A reader is designed for a particular areal density target, bandwidth, and with a certain SNR in mind. The reader SNR will depend on the targeted system SNR. By considering bandwidth and noise contributions described above, a minimum MR for a given RA product can be calculated for a certain sense current. Such MR-RA curves are shown in Fig. 24 [91]. Any point above the curve represents the usable range. The left side of the curve is mainly determined by spin-torque noise given by Eq. 15. The lower the spin-torque critical current density, the higher the required MR. The right side of the curve is mainly determined by shot noise and mag-noise given by Eqs. 11 and 14.

The aggressive increase in areal density has been assisted by continuous scaling of the distance between adjacent written tracks on the media. The adjacent track distance, measured in the number of tracks per inch (TPI) and referred to as the track density, is determined by a combination of the written track width, the read-back signal amplitude, and the reader $MRW_{50}$ (Fig. 18). The primary factors in the width and quality of the written track are the write head properties, the media, and the head-to-media spacing (fly height). The primary factors in the read-back signal are the physical dimensions of the read sensor, the read-head signal-to-noise ratio, the head-to-media spacing, and the accuracy of mechanically positioning the read head with respect to the written track.

The maximum track density for a given head/disk configuration is determined by measuring how far the read head can be moved offtrack or away from the center of the written track while the number of read-back errors stay below a predetermined level [92–94]. This offtrack performance is referred to as the offtrack capability (OTC).

To understand the OTC, a single written track in the absence of adjacent tracks should be considered first. As the read sensor moves offtrack, the read-back signal decreases and the noise from the disk increases, resulting in degraded read-back SNR. The number of read-back errors (error rate) increases as the read-back SNR decreases. When adjacent written tracks are included, then the OTC degrades compared to the isolated track case. With adjacent tracks, the main written track degrades when the newly written adjacent tracks begin overwriting portions of the main track. Additionally, with adjacent tracks, as the sensor is moved offtrack, the read-back signal will contain a signal from the main track and an interference signal from the adjacent track magnetization. A partially overwritten main track and side track interference signal (side reading) both reduce the read-back SNR as the sensor is moved offtrack.

Current track density targets are achieved with a write wide/read narrow scheme to provide performance margin and allowing for a guard band between the written tracks.

To determine an areal density, a "747 curve" is measured. The name "747 curve," as it suggests, stems from its shape resembling the outline of a 747 airplane. To prepare a 747 curve, first, two

DOI 10.1007/978-94-007-7604-3_35-1
© Springer Science+Business Media Dordrecht 2014

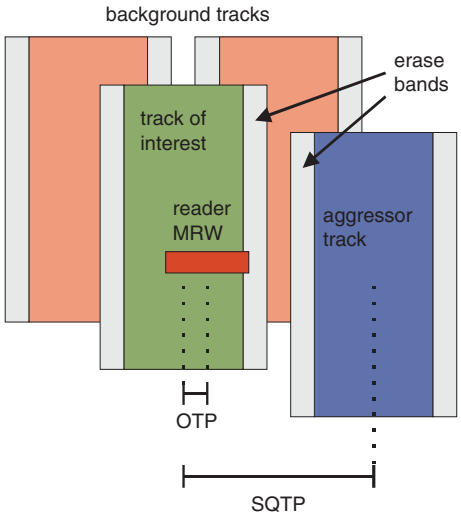


**Fig. 25** To determine offtrack capability (*OTC*) of a sensor, a track of interest is written over some background tracks. An aggressor track is written at a given squeeze track pitch offset (*SQTP*). The sensor is moved to an offtrack position (*OTP*) until the error rate drops below a predetermined level

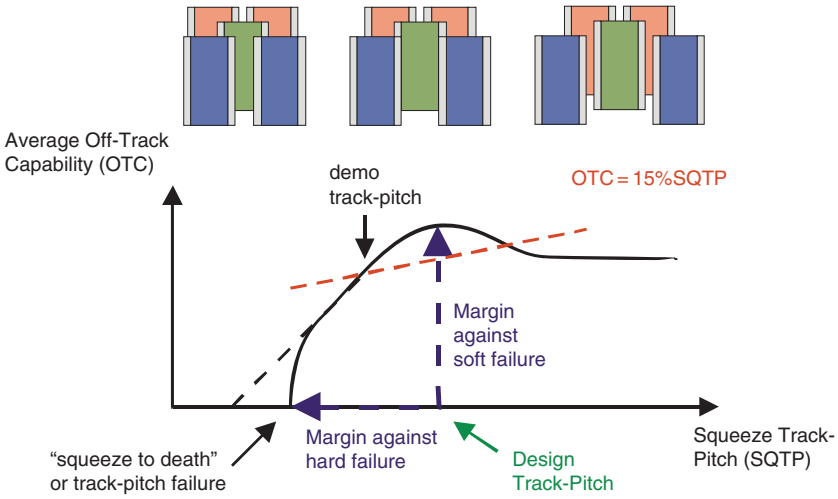


**Fig. 26** Schematic "747 curve" using two-sided squeeze outlining a predetermined error rate at a given OTC-SQTP combination. The design track pitch is the point of largest OTC. Margin against hard failure rate where the aggressor track is moved to a position where the track of interest cannot be read anymore and margin against soft error rate where the reader is moved to an offtrack position where information cannot be read anymore are indicated. For an areal density demonstration, a line at, for example, OTC = 15 % SQTP is drawn, and the intersection with the 747 curve at narrowest SQTP is called the demo track pitch

tracks are written with some offset to provide the background of old recorded information. Then the track of interest that is to be read back by the read head is written centered over the two underlying background tracks. Next, an aggressor track is written at an offset with respect to the previously recorded track of interest. The offset is commonly referred to as squeeze track pitch (SQTP). The data on the background tracks, the track of interest, and the aggressor track are all written at similar

DOI 10.1007/978-94-007-7604-3_35-1
© Springer Science+Business Media Dordrecht 2014

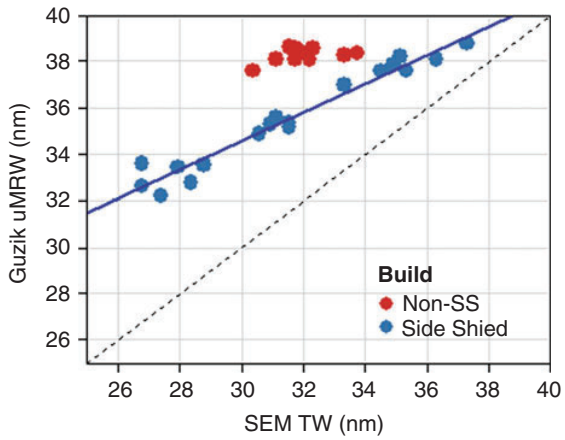


**Fig. 27** Magnetic versus physical track width at current read-sensor dimensions. The magnetic track width decreases at a rate significantly less than the physical track width. For read heads with side shields, the effect is less pronounced compared to non-side-shielded heads with hard-bias stabilization

bandwidth, so that the background and aggressor track data interferes with the data on the track of interest contributing to the read-back noise.

During the writing process, a band of the old information is erased at either side of the track. These erase bands are an artifact of the writer fringe fields and do not contain any data, but considerable noise. Their size depends on the details of the writing process and the disk magnetics.

After the track of interest and the aggressor track are written, the read sensor is positioned over the center of the track of interest and then moved to an offtrack position (OTP). The offtrack capability (OTC) of the reader at a given SQTP is determined by the distance the reader can be moved offtrack before the error rate drops below a predetermined acceptable level. The squeeze process is repeated and the OTC is determined as SQTP is reduced.

A schematic view of this process is shown in Fig. 25.

For sufficiently large SQTP, the written tracks do not interact and the OTC is independent of SQTP. As SQTP is reduced, the OTC at some point increases before it decreases. This is due to the aggressor track erase band erasing background track information at a bandwidth similar to the track of interest. Thus, the read-back noise is reduced and OTC increased compared to the large and narrow SQTP regime. At narrower SQTP, the data on the track of interest is overwritten with data from the aggressor track resulting in lower OTC.

When the OTC for a single-sided squeeze as described above is plotted against the SQTP, the shape curve is reminiscent of the cockpit and cabin of a Boeing 747; hence, these plots are referred to as “747 curves”. While traditionally a single-sided squeeze was used to prepare “747 curves”, more recently, a double-sided squeeze was adopted. A “747 curve” for such a double-sided squeeze is shown in Fig. 26. The track of interest recorded over two background tracks and being squeezed by the two aggressor tracks is schematically shown for various SQTP above the “747 curve.”

The design track pitch, and therefore the track density, is usually determined by choosing the point of largest OTC. The margin against hard failure rate is determined by the SQTP. It occurs when the aggressor track is moved to a position where the track of interest cannot be read anymore. The margin against soft error rate is determined by the reader OTP moving past the point of OTC where the reader cannot read anymore. For an areal density demonstration, a line at, for example, OTC = 15 % SQTP is drawn, and the intersection with the “747 curve” at narrowest SQTP is called the demo track pitch.

DOI 10.1007/978-94-007-7604-3_35-1
© Springer Science+Business Media Dordrecht 2014

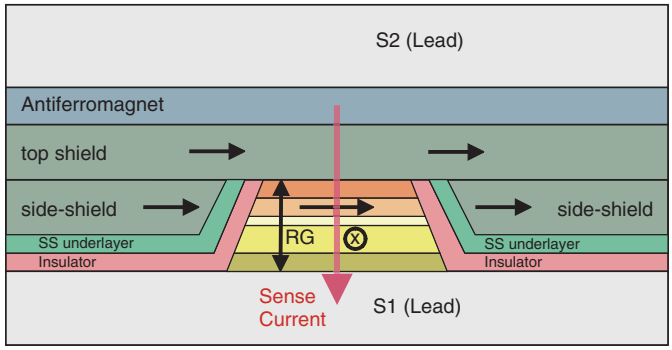


**Fig. 28** Schematic view of a read sensor using a coupled side- and top-shield structure. The top-shield structure is pinned by an antiferromagnetic layer for magnetic stability

"747 curves" are measured at various bit per inch (BPI) linear densities to determine areal density capability. BPI is a function of read-gap, head-media spacing, and media transition width as described by Eq. 3. Today, a bit aspect ratio of about width/length = 4:1 to 6:1 is used, which is a compromise to achieve high density, a good read-back performance with current head designs, and magnetic bit stability. The larger bit aspect ratio is used in server drives where BPI is higher and data rate is more at a premium compared to recording density.

## Outlook: Other Technologies

Current sensor track widths have now scaled into a regime where side reading has become much more dominant. One reason for the increased side reading is that due to minimum overcoat thickness requirements, the magnetic head-media spacing cannot be reduced at the same rate as lateral track width dimensions. Hence, as shown in Fig. 27, the sensor magnetic read width decreases at a rate significantly less than the physical track width.

To narrow this scaling divergence, the legacy hard bias is now being replaced by a side-shield structure [95] magnetically coupled to the top-shield structure as shown in Fig. 28. At narrow physical track width <40 nm, side-shield stabilized sensors yield a narrower sensor magnetic read width compared to that of hard-bias stabilized sensors as shown in Fig. 27. While the side shield is required to be permeable to act as a magnetic shield, it needs to be stable against reversal and exhibit a magnetization similar to the hard bias to act as a free layer stabilization. Further, its magnetostriction needs to be close to zero to avoid an additional anisotropy. Permalloy ($NiFe_{19}$) seems to be an obvious choice for a side-shield material due to its softness, high permeability, and low magnetostriction. Since a soft magnetic layer by itself would be prone to reversal due to the exposure to media fields and thermal agitation, the top-shield magnetization needs to be pinned by an antiferromagnetic layer. To improve thermal stability, an antiferromagnetically pinned structure similar to the one discussed for the read sensor rather than a simple pinned structure as shown in Fig. 28 may be utilized. One issue, however, is that the pinned top-shield structure needs to be set in a direction parallel to the ABS and thus perpendicular to the pinned layer direction of the sensor. Thus, the antiferromagnet used for the top shield can only be field annealed at a temperature significantly lower than the blocking temperature of the pinned layer structure of the sensor in order not to impact the sensor pinning direction. The thickness for the bottom and upper top-shield layers is chosen as a compromise in resolution and stability. While thinner layers increase magnetic stability, they lower down-track resolution due to increased top-shield stiffness and lower side-shield efficiency due to

DOI 10.1007/978-94-007-7604-3_35-1
© Springer Science+Business Media Dordrecht 2014

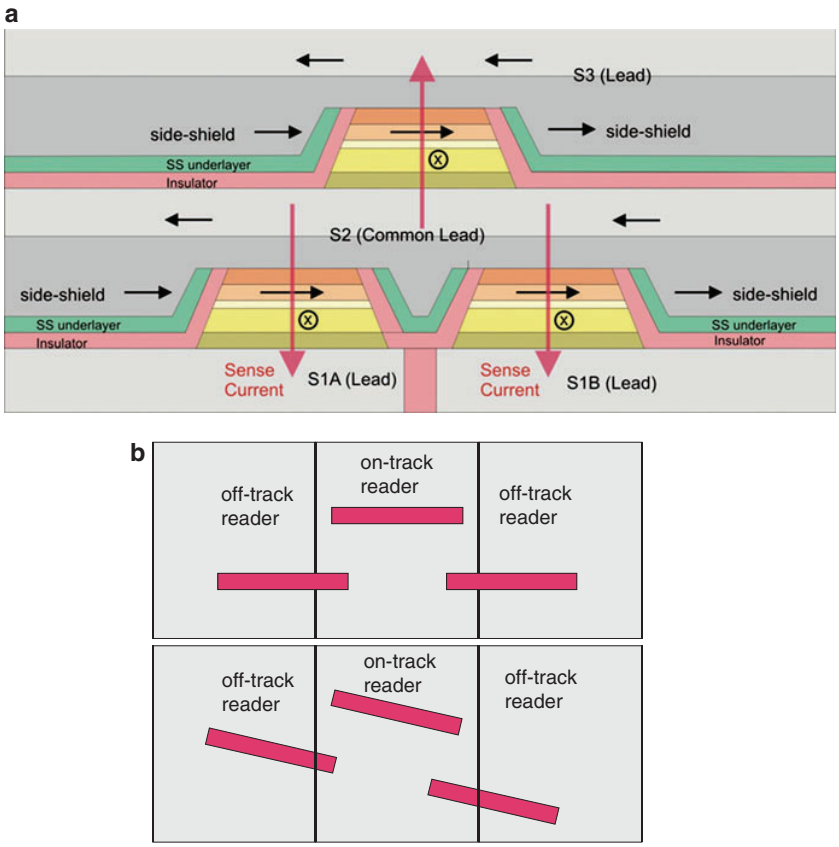


**Fig. 29** (**a**) Schematic view of a multitrack read sensor utilizing three read sensors. Two bottom read sensors are separated by about a track width, and a sensor located above and in the center of the two bottom read sensors is used for reading the center track to correct for side reading of the bottom sensors. (**b**) Positioning of the multitrack sensor with respect to the tracks, with a center on-track sensor and two offtrack sensors. As the recording head moves to the outer (or inner) diameter of the disk, one of the offtrack sensors moves closer to an on-track position due to skew

reduced side-shield permeability. Thicker layers on the other hand would improve down-track resolution and side-shield efficiency while lowering magnetic stability and thus make the coupled side- and top-shield structure prone to magnetic flipping.

Another future concept to increase areal density is two-dimensional magnetic recording (TDMR) where a multiple-read-sensor design is utilized to correct for side reading [96, 97]. An example of such a three-read-sensor TDMR design with two bottom sensors and one top sensor is shown in Fig. 29a. The two bottom sensors to correct for side reading are separated by less than a track width, and the third sensor for on-track reading is located above and in the center of the two bottom sensors. While the center (S2) and top shield (S3) would be common, the bottom shield (S1) could have to be split to electrically separate the sense currents of the two bottom sensors from each other. Obviously, such an advanced sensor concept bears many process and design challenges, such as the exact separation and placement of the sensors with respect to each other and the accommodation of extra electrical leads on small room, the definition of the magnetic bias points through the simultaneous magnetic stabilization of the pinned and free layers of all three sensors, and the design of some novel readout electronics. Figure 29b shows the basic concept of operation. While the center sensor reads the desired on-track information, the bottom sensors read a fraction of the on-track and offtrack information to correct for side reading and therefore effectively narrow the magnetic read width of

DOI 10.1007/978-94-007-7604-3_35-1
© Springer Science+Business Media Dordrecht 2014

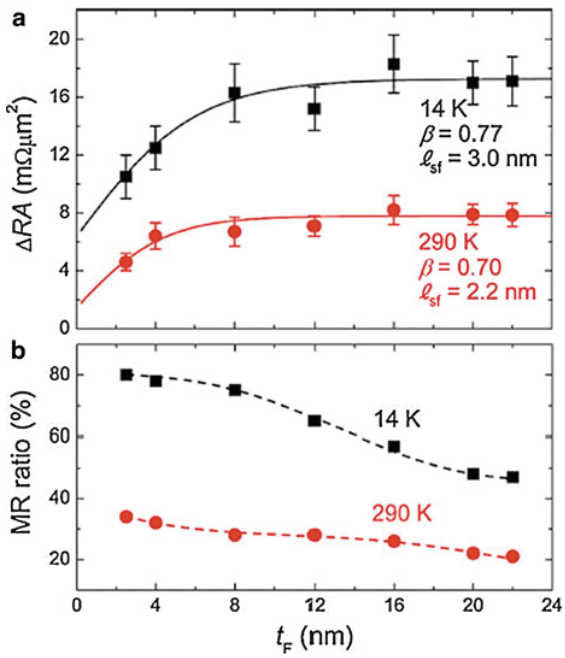


**Fig. 30** Variations of (**a**) ΔRA and (**b**) MR ratio for a CFAS/Ag/CFAS pseudo-spin valve for the CFAS layer thickness $t_f = 2.5–22$ nm at 14 K (*square*) and 290 K (*circle*). The fitted curve in (**a**) is by the Valet-Fert model (Reprinted with permission from Ref. [109]. Copyright (2011), AIP Publishing LLC)

the center on-track sensor. The narrower read width results in a reduced soft error rate and hence a higher recording density. As the recording head moves to the outer (or inner) diameter of the disk, one of the bottom sensors moves closer to an on-track position, the other farther into an offtrack position due to skew. In this scenario, side-reading correction is not optimal anymore, which further complicates soft error-rate correction on the inner and outer diameter of the disk.

Going forward, it will be challenging to maintain high signal-to-noise ratios along with high magnetic and thermal stability at ever smaller dimensions. As sensor cross sections diminish, the resistance of TMR sensors is increasing accordingly yielding a sensor impedance of several kΩ (see Fig. 17) which will attenuate the read-back signal at high data rate from the lower RC roll-off frequency, results in higher noise, and is incompatible with the high bandwidth amplifiers used in disk drives.

Lower RA products are mainly achieved by process and TMR stack improvements. Since present-day MgO barriers are already deposited at atomic layer thickness, their thickness cannot be reduced any further without pinholes to obtain lower RA products. Pinholes would give rise to ohmic current leakage resulting in reduced magneto-resistance and reliability issues. Thus, tunnel barrier materials with intrinsic RA products much lower than that of MgO need to be developed. However, despite ongoing research, no suitable barrier has been identified.

All-metal CPP giant magnetoresistive (GMR) sensors are an attractive follow-on reader technology to TMR sensors. With typical resistance-area products of ~0.05 Ω-μm$^2$, CPP-GMR sensors can exhibit low impedance and therefore low noise even at sensor dimensions below 30 nm. The structure of a CPP-GMR sensor is very similar to a TMR sensor however with the tunnel barrier replaced by a metallic spacer layer such as Cu or Ag. Rather than quantum mechanical tunneling across interfaces in a TMR sensors, the ΔR/R in CPP-GMR sensors is based on the spin-dependent scattering of electrons in the bulk and at the interfaces of the magnetic multilayer.

DOI 10.1007/978-94-007-7604-3_35-1
© Springer Science+Business Media Dordrecht 2014

Among the challenges that CPP-GMR sensors face are low signal levels due to their low resistance, low ΔR/R for thin magnetic layers, as well as current-induced noise and magnetic instability from spin-torque effects, which arise from a spin-polarized electron current interacting with the magnetization of the electrodes resulting in a torque on the magnetization.

Valet and Fert developed a comprehensive model describing CPP-GMR transport [98]. Important parameters describing the CPP-GMR effect are the bulk ($\beta$) and interface ($\gamma$) scattering parameters of the magnetic layers; the resistivity and spin-diffusion length, $l_{SF}$, of the magnetic and spacer layers; as well as the interface resistance between magnetic and spacer layers. The spin-diffusion length is an important scaling parameter. For practical applications, the spin-diffusion length of the spacer layer needs to be long compared to its thickness, so that electrons maintain their spin polarization as they flow between the free and reference layers, and the spin-diffusion length of the magnetic layers needs to be short compared to their respective thicknesses, so that spin-polarized electrons scatter effectively within the layer thickness of the reference and free layers.

However, while the spin-diffusion length of common spacer layers such as Cu and Ag is several 100 nm, much longer than the typical spacer layer thickness of ~3–5 nm, the spin-diffusion length of common magnetic materials is much longer than the typical layer thickness of ~3–5 nm in a CPP-GMR spin valve. The typical magnetic layer thickness is limited by factors like the available shield-to-shield spacing determining resolution, the pinning strength which decreases with layer thickness, and the free layer moment that needs to be matched to the media. In the practical limit of the layer thickness much thinner than the spin-diffusion length, the Valet-Fert equations can be simplified into a parallel resistor network model for spin-up and spin-down spins [99–101]. For a spin-valve comprising a free, reference, and pinned layer, the ΔRA product is given by [102]

$$\Delta RA = \frac{4\left(\beta_F \rho_F^* t_F + 2\gamma R_{F/N}^* A\right)\left(\beta_R \rho_R^* t_R - \beta_P \rho_P^* t_P + \gamma R_{F/N}^* A\right)}{\beta_F t_F + \beta_R t_R + \beta_P t_P + R_{F/N}^* A + R_{\text{para}}} \tag{16}$$

where $\beta_i$ and $\gamma_i$ are the bulk and interface spin-scattering coefficients, respectively; $t_i$ is the thickness of the layers; $\rho_i^* = \rho_i/(1 - \beta_i^2)$ where $\rho_i$ is the resistivity of the layers; and $R_{ij}^*A = R_{ij}A/(1 - \gamma^2)$ where $R_{ij}A$ is the resistance-area product at the interface between magnetic and spacer layers. The suffixes $i,j = F$, $R$, and $P$ indicate the free, reference, and pinned layers, respectively. $R_{\text{para}}$ is the parasitic serial resistance in the stack (e.g., from the antiferromagnet, seed and cap layers). Obviously high bulk and interface spin-scattering efficiency (high β and γ) and ferromagnetic layer and interface resistances lead to high ΔRA

Although high CPP-GMR can be achieved in thick multilayers, only small GMR values of ~3 % [103, 104] were obtained in early versions of CPP-GMR spin valves using conventional materials like CoFe, NiFe, and Cu with practical layer thickness. More recently, GMR has improved with the use of improved materials, such as highly spin-polarized Heusler alloys like $Co_2MnGe$ or $Co_2MnSi$ [105–107] or other CoFe-based ternary alloys like CoFeAl or CoFeGe [102, 108]. These alloys exhibit high bulk and interface scattering parameters and short spin-diffusion length yielding high GMR. Still, further improvement in GMR is required to meet requirements for future >1 TBit/in$^2$ sensors. Recently, room-temperature GMR values of ~18 % have been reported on epitaxially grown CPP-GMR stacks on MgO utilizing highly spin-polarized $Co_2FeAl_{0.5}Si_{0.5}$ (CFAS) Heusler alloys and Ag spacers [109]. While the annealing was performed at a reasonable temperature of 300 ºC, epitaxial stacks and the relatively thick layers used are not compatible with the manufacturing process of recording heads. Similarly, using an even higher annealing temperature of 450 ºC and incompatible thick layers of $L2_1$-ordered $CoFe_{0.5}Mn_{0.5}Si$ Heusler alloys and Ag spacers, GMR in

DOI 10.1007/978-94-007-7604-3_35-1
© Springer Science+Business Media Dordrecht 2014

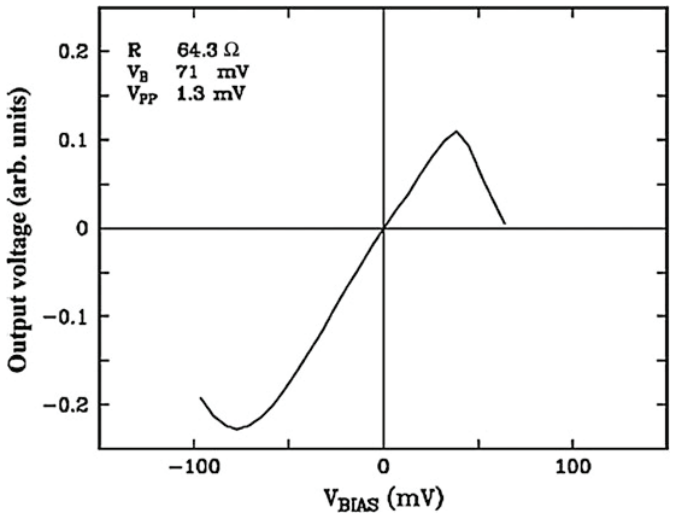


**Fig. 31** CPP-GMR sensor output voltage as a function of bias voltage. The largest output is obtained for a bias of ∼75 mV. The output decrease at below −75 mV and above 40 mV is due to spin-torque instabilities (© [2008] IEEE. Reprinted with permission from Ref. [106])

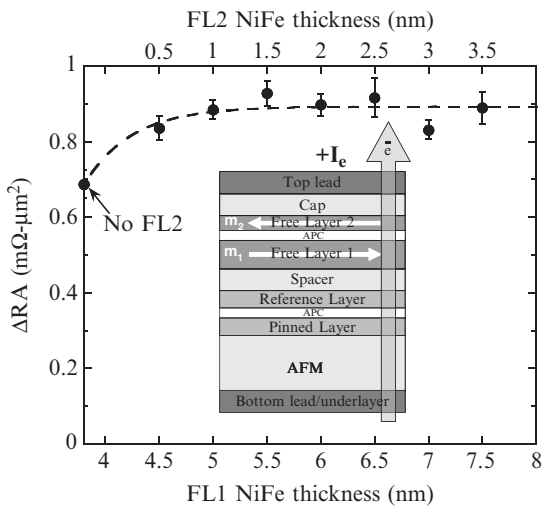


**Fig. 32** ΔRA versus NiFe thickness in FL1 (*bottom axis*) or FL2 (*top axis*). *Inset*: spin-valve structure with antiparallel pinned free layer (Reprinted with permission from Ref. [117]. Copyright (2008), AIP Publishing LLC)

excess of 70 % has been observed [110]. Nevertheless, these studies demonstrate how improvement in materials may ultimately lead to practical CPP-GMR sensors. As an example, the ΔRA product for varying free layer thickness in a pseudo-spin valve (no antiferromagnet and pinned layer) with CFAS Heusler alloy free and reference layers is shown for 14 K and 290 K in Fig. 30a. The bulk spin-scattering coefficient β and the spin-diffusion length $l_{SF}$ are derived from fitting the data to equations for the Valet-Fert model. The observed β is considerably higher than for standard materials like Co (β ∼ 0.48 at 4 K [93], β ∼ 0.36 at 77 K [101]) and results in the high MR >30 % at room temperature and ∼80 % at 14 K. β and γ (not shown) decrease, while the parasitic resistances increase with temperature resulting in the large drop in MR as temperature is increased as shown in

DOI 10.1007/978-94-007-7604-3_35-1
© Springer Science+Business Media Dordrecht 2014

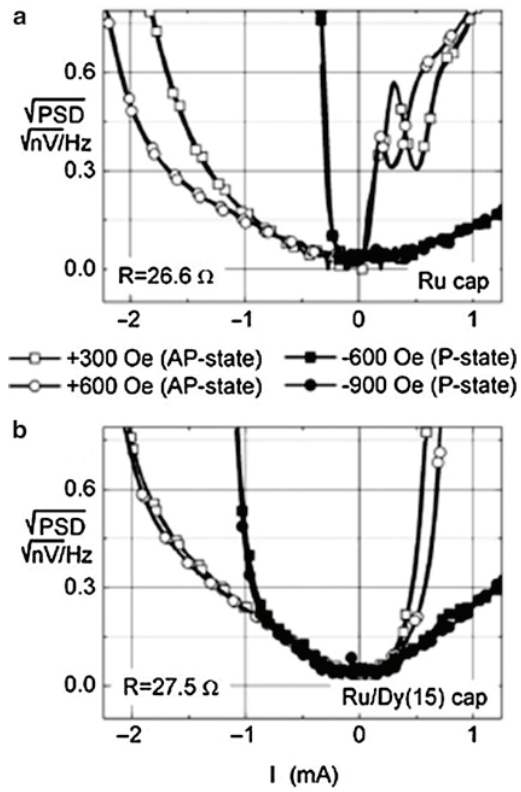


**Fig. 33** Measured power spectrum density for a CPP-GMR spin valve in the parallel and antiparallel states, both for positive and negative current polarities. The threshold current increases by adding a Dy cap providing higher damping to the free layer (Reprinted with permission from Ref. [119]. Copyright (2008), AIP Publishing LLC)

Fig. 30b. The short $l_{SF}$ of ~2–3 nm is on the order of a typical layer thickness in spin valves, and mild annealing temperatures make CFAS an interesting material for applications. For comparison, the $l_{SF}$ of Co is ~44 nm at 4 K [101].

Another serious limitation for CPP-GMR devices is their high susceptibility to spin-torque instabilities due to their low resistance. The dilemma is that highly spin-polarized alloys are required to obtain high GMR values, but that highly, but the highly spin-polarized alloys exhibit low damping [111–114] as spin-polarized electrons only have one channel to relax. As can be seen from high spin polarization and low damping lower the critical current density for spin-torque instabilities. Thus, extrinsic solutions to this spin-torque dilemma are needed. The output voltage of a Heusler-based CPP-GMR spin valve is shown in Fig. 31. The output voltage decreases above a certain bias voltage due to spin-torque-induced instabilities.

Various schemes to increase the threshold current against spin-torque instability of the free layer have been proposed. The stability can be improved using dual spin valves due to their symmetry [115, 116]; however, these are impractical as they have a much wider read gap due to their two pinned layer structures compared to conventional spin valves with a single pinned layer structure. Antiparallel coupled free layers provide from Eq. 15, higher stability against spin-torque instabilities due to the reduced net free layer moment $M \cdot t = M_{FL1} \cdot t_{FL1} - M_{FL2} t_{FL2}$ [117], where the subscripts *FL1* and *FL2* indicate the lower and upper free layers, respectively. The antiparallel coupled free layers also exhibit the advantage that *FL1* can be made thicker than a single *FL* since part of its moment is canceled by *FL2*, thus leading to higher GMR as shown in Fig. 32.

DOI 10.1007/978-94-007-7604-3_35-1
© Springer Science+Business Media Dordrecht 2014

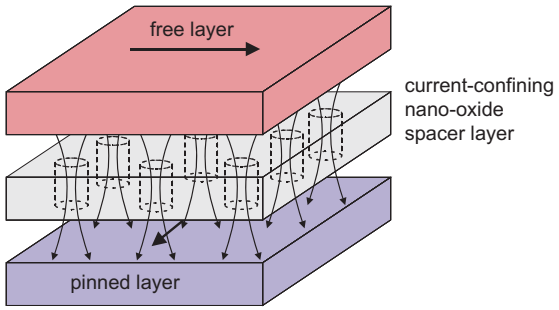


**Fig. 34** Schematic picture of a CCP-CPP spin valve. Current is confined by the nano-oxide layer inside the spacer layer

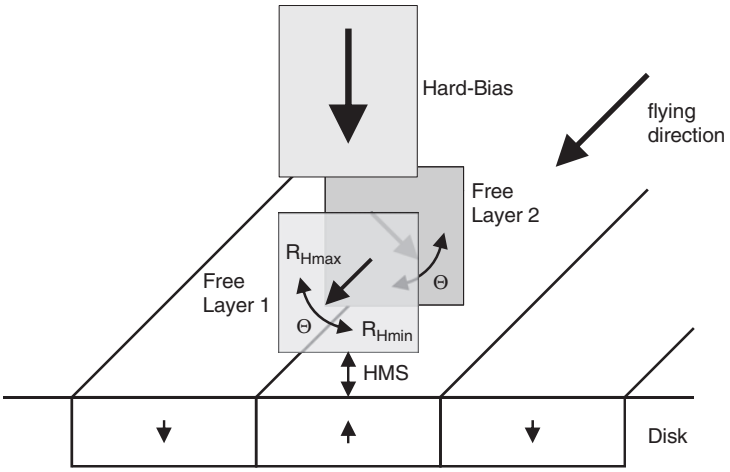


**Fig. 35** Scissor sensor comprising two free layers. The free layer magnetization is stabilized by a hard bias located at the back of the stripe rather than at each side of the track width

Since the critical current density against spin-torque instabilities is proportional to the magnetic damping constant, increasing the magnetic damping constant in the free layer is an obvious solution. While it is possible to greatly increase the magnetic damping through alloying with a material that exhibits high spin-orbit coupling, e.g., a rare earth material [118], it results in a loss of moment and most likely results in lower spin polarization. A more practical approach is to add a rare earth layer (e.g., Dy) to the sensor cap [119]. Figure 33 shows the measured power spectrum density for a CPP-GMR spin valve in the parallel and antiparallel states, both for positive and negative current polarities. The critical current increases about threefold by adding a Dy cap that provides higher damping to the free layer.

To bridge the gap between TMR sensors exhibiting RA products of 0.5 to 1 Ω-μm$^2$ and CPP sensors exhibiting RA products of 0.05 to 0.1 Ω-μm$^2$, CPP sensors with current confined path (CCP) have been proposed [120–123]. These sensors have a nano-oxide layer with pinholes inserted somewhere in the metallic spacer layer (Fig. 34), for example, an Al oxide, CoFe oxide, or ZnO layer in a Cu spacer. The current is constricted to flow through the pinholes of the nano-oxide layer resulting in an increase in both RA and ΔRA products. However, it would be challenging to manufacture these partially oxidized metal spacer layers with consistent properties, in particular achieving nano-oxide layers with the same size- and spatial distribution of nano-holes.

DOI 10.1007/978-94-007-7604-3_35-1
© Springer Science+Business Media Dordrecht 2014

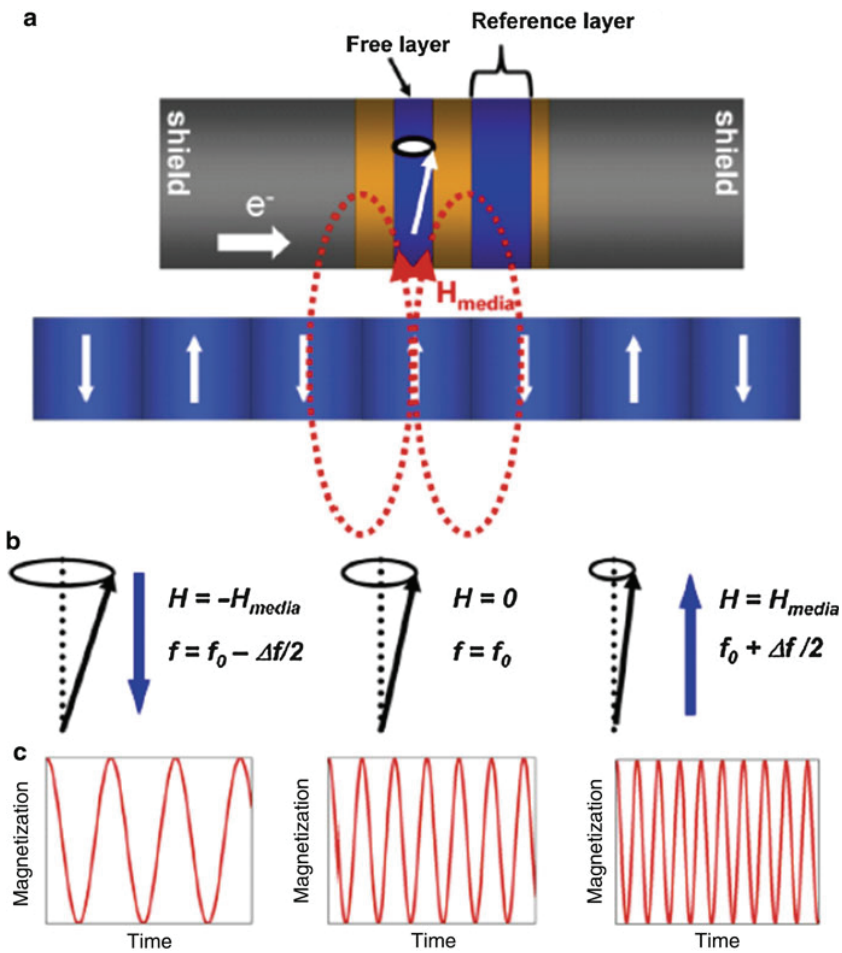


**Fig. 36** (**a**) Schematic view of a spin-torque oscillator with a spin-valve structure in between two magnetic shields. (**b**) Transitions in the magnetic media cause fluctuations in the magnetic field sensed by the free layer, which cause a change in the free layer magnetization precession orbit. (**c**) These changes in precession orbit can be detected as a shift in frequency (© IOP Publishing. Reproduced from [124] with permission from IOP Publishing. All rights reserved)

Another sensor under consideration for ultra-narrow read gaps is a trilayer scissor sensor shown in Fig. 35. The scissor sensor only contains two magnetic free layers separated by either a tunnel barrier in the case of a TMR-based scissor sensor or a metallic spacer layer in the case of a CPP-GMR-based scissor sensor. The two free layers are stabilized by a hard bias located in the back of the sensor. The field from the hard bias, the interlayer coupling field, and the demagnetization fields of the layers are balanced so that the magnetization of the two layers is directed to about +/−45º from the ABS, thus being about perpendicular to each other. Magnetic field excitation will result in small angle rotation of both layers toward or apart from each other, i.e., a scissoring motion. Since both layers rotate in opposite directions at the same time, small fields will result in high utilization. As simple and promising as the concept appears, the difficulty is to stabilize each free layer in an appropriate state with the hard bias. Unlike a conventional TMR sensor, no unidirectional anisotropy keeps a reference in place, and the hard bias needs to stabilize two rather than one layer. Both layers may interchange magnetization direction resulting in the same energy which will be a source of telegraph and hence $1/f^{\eta}$ noise. Moreover, a uniform rotation mode of both layer magnetizations will not yield any MR, but only add to the noise.

DOI 10.1007/978-94-007-7604-3_35-1
© Springer Science+Business Media Dordrecht 2014

Yet another proposed reader technology is the use of a spin-torque oscillator as sensor, which would detect the transitions in the magnetic media as changes of the precession frequency of the free layer [124]. A spin-torque oscillator with a spin-valve structure between two magnetic shields is shown in Fig. 36a. While the direction of the reference layer magnetization is fixed parallel to the ABS by exchange biasing, the free layer is oscillating due to the applied sensor current being above the critical current density limit for spin-torque instabilities. While the free layer main magnetization axis is kept perpendicular to the ABS, transitions in the media cause the precession orbit of the free layer magnetization to change and thereby induce a shift in resonance frequency as shown in Fig. 36b and c. As the precession orbit closes down (opens up) the free layer, precession frequency increases (decreases). Similar materials as for a CPP-GMR sensor can be used, as high spin polarization leads to low damping and to a low critical spin-torque current density; however, for a spin-torque sensor, narrow linewidth and large frequency shifts rather than high GMR are needed. The advantage of this approach over a CPP-GMR sensor is that spin-torque instabilities are turned from noise to signal; however, it will be challenging to stabilize the free layer magnetization orbits in a controlled manner to obtain narrow linewidth and sufficient output signal. As for CPP-GMR, additional materials research and development is needed.

## Summary

In conclusion, the physics and design of modern magnetic recording read heads utilizing the tunnel magnetoresistive effect has been discussed. For this, the underlying principles of thin film magnetism and electron transport in nanostructures has been discussed, and various concepts such as device scaling, stabilization, signal-to-noise considerations, and read-back performance have been explained. An outlook on possible future technologies has been given, but it is yet to be determined if any of these new technologies will replace TMR sensors any time soon. Introduction of any of these new technologies will greatly depend on many aspects, such as if a tunnel barrier with an intrinsically lower RA product than MgO while delivering high MR can be identified or if any significant progress in the synthesis of new highly polarized materials can be made for CPP-GMR and if spin-torque noise can be contained at the same time. For scissor and spin-torque sensors, magnetic stabilization will be the greatest challenge.

## References

1. Grochowski E (2012) 2012 HDD capital equipment and technology report, Coughlin Associates
2. Binasch G, Grünberg P, Saurenbach F, Zinn F (1989) Enhanced magnetoresistance in layered magnetic structures with antiferromagnetic interlayer exchange. Phys Rev B 39:4828–4830
3. Baibich MN, Broto JM, Fert A, Nguyen Van Dau F, Petroff F, Etienne P, Creuzet G, Friedrich A, Chazelas J (1988) Giant magnetoresistance of (001)Fe/(001) Cr magnetic superlattices. Phys Rev Lett 61:2472–2475
4. Parkin SSP, Bhadra B, Roche KP (1991) Oscillatory magnetic exchange coupling through thin copper layers. Phys Rev Lett 66:2152–2155
5. Dieny B, Speriosu VS, Parkin SSP, Gurney BA, Wilhoit DA, Mauri D (1991) Giant magnetoresistance in soft ferromagnetic multilayers. J Appl Phys 43:1297–1300

DOI 10.1007/978-94-007-7604-3_35-1
© Springer Science+Business Media Dordrecht 2014


6. Heim DE, Fontana RE, Tsang C, Speriosu VS, Gurney BA, Williams ML (1994) Design and operation of spin valve sensors. IEEE Trans Magn 30:316–321
7. Tsang C, Fontana RE, Lin T, Heim DE, Speriosu VS, Gurney BA, Williams ML (1994) Design fabrication & testing of spin-valve read heads for high density recording. IEEE Trans Magn 30:3801–3806
8. Hong J, Noma K, Kanda E, Kanai H (2003) Very large giant magnetoresistance of spin valves with specularly reflective oxide layers. Appl Phys Lett 83:960–962
9. Kools JCS (1996) Exchange-biased spin-valves for magnetic storage. IEEE Trans Magn 32:3165–3184
10. Childress JA, Fontana RE (2005) Magnetic recording read head sensor technology. CR Physique 6:997–1012
11. Mee CD, Daniel ED (1995) Magnetic recording technology, 2nd edn. McGraw-Hill, New York
12. Julliere M (1975) Tunneling between ferromagnetic films. Phys Lett 54A:225–226
13. Mac Laren JM, Zhang XG, Butler WH (1997) Validity of the Julliere model of spin-dependent tunneling. Phys Rev B 56:11827–11832
14. Parker JS, Watts SM, Ivanov PG, Xiong P (2002) Spin polarization of $CrO_2$ at and across an artificial barrier. Phys Rev Lett 88:196601
15. Bullen H, Garrett SJ (2002) Epitaxial growth of $CrO_2$ thin films on $TiO_2$(110) surfaces. Chem Mater 14:243–248
16. Umetsu RY, Kobayashi K, Fujita A, Kainuma R, Ishida K (2008) Phase stability and magnetic properties of L21 phase in $Co_2Mn(Al_{1-x}Si_x)$ heusler alloys. Scr Mater 58:723–726
17. Ishikawa T, Liu H, Taira T, Matsuda K, Uemura T, Yamamoto M (2009) Influence of film composition in $Co_2MnSi$ electrodes on tunnel magnetoresistance characteristics of $Co_2MnSi/MgO/Co_2MnSi$ magnetic tunnel junctions. Appl Phys Lett 95:232512
18. Miyazaki T, Tezuka N (1995) Giant magnetic tunneling effect in $Fe/Al_2O_3/Fe$ junction. J Magn Magn Mater 139:L231–L234
19. Moodera JS, Kinder LR, Wong TM, Meservey R (1995) Large magnetoresistance at room temperature in ferromagnetic thin film tunnel junctions. Phys Rev Lett 74:3273–3276
20. Sakuraba Y, Nakata J, Oogane M, Kubota H, Ando Y, Sakuma A, Miyazaki T (2005) Huge spin-polarization of L21-ordered $Co_2MnSi$ epitaxial heusler alloy film. Jpn J Appl Phys 44: L1100–L1102
21. Okamura S, Miyazaki A, Sugimoto S, Tezuka N, Inomata K (2005) Large tunnel magnetoresistance at room temperature with a $Co_2FeAl$ full-heusler alloy electrode. Appl Phys Lett 86:232503
22. Oogane M, Shinano M, Sakuraba Y, Ando Y (2009) Tunnel magnetoresistance effect in magnetic tunnel junctions using epitaxial $Co_2FeSi$ Heusler alloy electrode. J Appl Phys 105:07C903
23. Butler WH, Zhang XG, Schulthess TC, MacLaren JM (2001) Spin-dependent tunneling conductance of Fe/MgO/Fe sandwiches. Phys Rev B 63:054416
24. Mathon J, Umerski A (2001) Theory of tunneling magnetoresistance of an epitaxial Fe/MgO/Fe (001) junction. Phys Rev B 63:220403(R)
25. Zhang XG, Butler WH (2004) Large magnetoresistance in bcc Co/MgO/Co and FeCo/MgO/FeCo tunnel junctions. Phys Rev B 70:172407
26. Parkin SSP, Kaiser C, Pachula A, Rice PM, Samant M, Yang SH (2004) Giant tunnelling magnetoresistance at room temperature with MgO (100) tunnel barriers. Nature 3:862–867

DOI 10.1007/978-94-007-7604-3_35-1
© Springer Science+Business Media Dordrecht 2014

27. Yuasa S, Nagahama T, Fukushima A, Suzuki Y, Ando K (2004) Giant room-temperature magnetoresistance in single-crystal Fe/MgO/Fe magnetic tunnel junctions. Nature 3:868–871
28. Djayaprawira DD, Tsunegawa K, Nagai M, Maehara H, Yamagata S, Watanabe N, Yuasa S, Suzuki Y, Ando K (2005) 230% room-temperature magnetoresistance in CoFeB/MgO/CoFeB magnetic tunnel junctions. Appl Phys Lett 86:092502
29. Nagamine Y, Maehara H, Tsunegawa K, Djayaprawira DD, Watanabe N (2006) Ultralow resistance-area product of $0.4\Omega(\mu m)^2$ and high magnetoresistance above 50 % in CoFeB/MgO/CoFeB magnetic tunnel junctions. Appl Phys Lett 89:162507
30. Lee YM, Hayakawa J, Ikeda S, Matsukura F, Ohno H (2007) Effect of electrode composition on the tunnel magnetoresistance of pseudo-spin-valve magnetic tunnel junction with a MgO tunnel barrier. Appl Phys Lett 90:212507
31. Bonell F, Hauet T, Andrieu S, Bertran F, Le Fe`vre P, Calmels L, Tejeda A, Montaigne F, Warot-Fonrose B, Belhadji B, Nicolaou A, Taleb-Ibrahimi (2012) A Spin-Polarized Electron Tunneling in bcc FeCo/MgO/FeCo (001) Magnetic Tunnel Junctions. Phys Rev Lett 108:176602-1–176602-5
32. Nogues J, Schuller IK (1999) Exchange bias. J Magn Magn Mater 192:203–232
33. Fuke H, Saito K, Kamiguchi Y, Iwasaki H, Sahashi M (1997) Spin-valve giant magnetoresistive films with antiferromagnetic Ir-Mn layers. J Appl Phys 81:4004–4006
34. van Driel J, Coehoorn R, Lenssen KMH, Kuiper AET, de Boer FR (1999) Thermal stability of Ir–Mn as exchange biasing material. J Appl Phys 85:5522–5524
35. van Driel J, de Boer FR, Lenssen KMH, Coehoorn R (2000) Exchange biasing by Ir19Mn81: dependence on temperature, microstructure and antiferromagnetic layer thickness. J Appl Phys 88:975–982
36. Tsunoda M, Takahashi H, Takahashi M (2009) Systematic study for magnetization dependence of exchange anisotropy strength in Mn-Ir/FM (FM=Ni-Co, Co-Fe, Fe-Ni) bilayer system. IEEE Trans Magn 45:3877–3880
37. van den Berg HAM, Clemens W, Gieres G, Rupp G, Schelter W, Vieth M (1996) GMR sensor scheme with artificial antiferromagnetic subsystem. IEEE Trans Magn 32:4624–4626
38. Huai Y, Zhang J, Anderson GW, Rana P, Funada S, Hung CY, Zhao M, Tran S (1999) Spin-valve heads with synthetic antiferromagnet CoFe/Ru/CoFe/IrMn. J Appl Phys 85:5528–5530
39. Ruderman MA, Kittel C (1954) Indirect exchange coupling of nuclear moments by conduction electrons. Phys Rev 96:99–102
40. Kasuya T (1956) A Theory of Metallic Ferro- and Antiferromagnetism on Zener's Model. Prog Theory Phys 16:45–57
41. Yosida K (1957) Magnetic properties of Mn-Cu alloys. Phys Rev 106:893–898
42. Bruno P, Chapert C (1991) Oscillatory coupling between ferromagnetic layers separated by a nonmagnetic metal spacer. Phys Rev Lett 67:1602–1605 and Erratum (1991) Phys Rev Lett 67:2592
43. Bruno P, Chapert C (1992) Ruderman-kittel theory of oscillatory interlayer exchange coupling. Phys Rev B 46:261–270
44. Mathon J, Villeret M, Edwards DM (1992) Exchange coupling in magnetic multilayers: effect of partial confinement of carriers. J Phys Condens Mattter 4:9873–9892
45. Parkin SSP, More N, Roche KP (1990) Oscillations in exchange coupling and magnetoresistance in metallic superlattice structures: Co/Ru, Co/Cr, and Fe/Cr. Phys Rev Lett 64:2304–2307

DOI 10.1007/978-94-007-7604-3_35-1
© Springer Science+Business Media Dordrecht 2014

46. Parkin SSP (1991) Systematic variation of the strength and oscillation period of indirect magnetic exchange coupling through the 3d, 4d, and Sd transition metals. Phys Rev Lett 67:3598–3601
47. Slonczewski JC (1991) Fluctuation mechanism for biquadratic exchange coupling in magnetic multilayers. Phys Rev Lett 67:3172–3175
48. Filipkowski ME, Krebs JJ, Prinz GA, Gutierrez CJ (1995) Giant near-90° coupling in epitaxial CoFe/Mn/CoFe sandwich structures. Phys Rev Lett 75:1847–1850
49. Bobo JF, Kikuchi H, Redon O, Snoeck E, Piecuch M, While RL (1999) Pinholes in antiferromagnetically coupled multilayers: effect on hysteresis loops and relation to biquadratic exchange. Phys Rev B 90:4131–4141
50. Demokritov SO (1998) Biquadratic interlayer coupling in layered magnetic systems. J Phys D Appl Phys 31:925–941
51. Beach RS, Pinarbasi M, Carey MJ (2000) AP-pinned spin valve GMR and magnetization. J Appl Phys 87:5723–5725
52. Dimitrov DV, van Ek J, Li YF, Xiao JQ (2000) Enhanced magnetic stability in spin valves with synthetic antiferromagnet. J Appl Phys 87:6427–6429
53. Bilzer C, Devolder T, Kim JV, Counil G, Chappert C, Cardoso S, Freitas PP (2006) Study of the dynamic magnetic properties of soft CoFeB films. J Appl Phys 100:053903
54. Tsunegawa K, Djayaprawira DD, Nagai M, Maehara H, Yamagata S, Watanabe N (2005) Giant tunneling magnetoresistance effect in low-resistance CoFeB/MgO(001)/CoFeB magnetic tunnel junctions for read-head applications. Appl Phys Lett 87:072503
55. Hayakawa J, Ikeda S, Lee YM, Matsukura F, Ohno H (2006) Effect of high annealing temperature on giant tunnel magnetoresistance ratio of CoFeB/MgO/CoFeB magnetic tunnel junctions. Appl Phys Lett 89:232510
56. Cha JJ, Read JC, Buhrman RA, Muller DA (2007) Spatially resolved electron energy-loss spectroscopy of electron-beam grown and sputtered CoFeB/MgO/CoFeB magnetic tunnel junctions. Appl Phys Lett 91:062516
57. Cha JJ, Read JC, Egelhoff WF, Huang PY, Tseng HW, Li Y, Buhrman RA, Muller DA (2009) Atomic-scale spectroscopic imaging of CoFeB/Mg–B–O/CoFeB magnetic tunnel junctions. Appl Phys Lett 95:032506
58. Tezuka N, Ikeda N, Sugimoto S, Inomata K (2007) Giant tunnel magnetoresistance at room temperature for junctions using full-heusler Co2FeAl0:5Si0:5 electrodes. Jpn J Appl Phys 46: L454–L456
59. Singleton EW, Narayan PB, Xiong W, Raman R, Hoo HL (1999) Effects of Cr, CrV, and CrTi underlayers on magnetic, structural, and materials reliability properties of CoPt thin films. J Appl Phys 85:5840–5842
60. Worledge DC, Trouilloud PL (2003) Magnetoresistance measurement of unpatterned magnetic tunnel junction wafers by current-in-plane tunneling. Appl Phys Lett 83:84–86
61. Bertram HN (1994) Theory of magnetic recording. Cambridge University Press, Cambridge, UK, p 133
62. Mächtle P, Berger R, Dietzel A, Despont M, Häberle W, Stutz R, Binnig G K, Vettiger P (2001) Integrated microheaters for in-situ flying-Height control of sliders used in hard-disk drives. In: The 14th IEEE international conference on micro electro mechanical systems (MEMS), pp 196–199
63. Leal JL, Kryder MH (1996) Interlayer coupling in spin valve structures. IEEE Trans Magn 32:4642–4644

DOI 10.1007/978-94-007-7604-3_35-1
© Springer Science+Business Media Dordrecht 2014


64. Kools JCS, Kula W, Mauri D, Lin T (1999) Effect of finite magnetic film thickness on néel coupling in spin valves. J Appl Phys 85:4466–4468
65. Jin Z, Bertram N (2008) A simple model for optimal read width due to finite write width and offtrack interference. IEEE Trans Magn 44:3384
66. Wang L, Patwari MS, Stokes SW (2011) Modeling of 1/f noise due to thermally induced magnetic switches of antiferromagnetic grains in magnetic tunneling readers. J Appl Phys 109:07B725
67. Lei ZQ, Li GJ, Egelhoff WF Jr, Lai PT, Pong PWT (2011) Review of noise sources in magnetic tunnel junction sensors. IEEE Trans Magn 47:602–612
68. Klaassen KB, van Peppen JCL, Xing X (2003) Noise in magnetic tunnel junction devices. J Appl Phys 93:8573–8575
69. Klaassen KB, Xing X, van Peppen JCL (2004) Signal and noise aspects of magnetic tunnel junction sensors for data storage. IEEE Trans Magn 40:195–202
70. Keshner MS (1982) 1/f Noise. Proc IEEE 70:212–218
71. Christensson S, Lundström I, Svensson C (1968) Low frequency noise in MOS transistors – I theory. Solid State Electron 11:797–812
72. Stearrett R, Wang WG, Shah LR, Xiao JQ, Nowak ER (2010) Magnetic noise evolution in CoFeB/MgO/CoFeB tunnel junctions during annealing. Appl Phys Lett 97:243502
73. Md Nor AF, Kato T, Ahn SJ, Daibou T, Ono K, Oogane M, Ando Y, Miyazaki T (2006) Low-frequency noise in MgO magnetic tunnel junctions. J Appl Phys 99(08):T306
74. Machlup S (1954) Noise in semiconductors: spectrum of a two-parameter random signal. J Appl Phys 25:341
75. Klaassen KB, Taratorin A (2007) Is electrical 1/f noise in tunneling magnetoresistive heads a form of equilibrium noise? IEEE Trans Magn 43:2193–2195
76. Liu F, Ding Y, Kemshetti R, Davies K, Rana P, Mao S (2009) Electrical low frequency random telegraph noise in magnetic tunnel junctions. J Appl Phys 105:07C927
77. Smith N, Arnett P (2001) White-noise magnetization fluctuations in magnetoresistive heads. Appl Phys Lett 78:1448–1450
78. Smith N, Arnett P (2002) Thermal magnetization noise in spin valves. IEEE Trans Magn 38:32–37
79. Jury JC, Klaassen KB, van Peppen JCL, Wang SX (2002) Measurement and analysis of noise sources in giant magnetoresistive sensors up to 6 GHz. IEEE Trans Magn 38:3545–3555
80. Smith N, Carey MJ, Childress JR (2010) Measurement of Gilbert damping parameters in nanoscale CPP-GMR spin valves. Phys Rev B 81:184431
81. Taratorin A (2009) Measurement of effective free layer magnetization orientation of TMR sensors. IEEE Trans Magn 45:3449–3452
82. Berger L (1996) Emission of spin waves by a magnetic multilayer traversed by a current. Phys Rev B 54:9353–9358
83. Slonczewski JC (1996) Current-driven excitation of magnetic multilayers. J Magn Magn Mater 159:L1–L7
84. Tsoi M, Jansen AG, Bass J, Chiang WC, Seck M, Tsoi V, Wyder P (1998) Excitation of a magnetic multilayer by an electric current. Phys Rev Lett 80:4281–4284, erratum Phys Rev Lett 81:493
85. Katine JA, Albert FJ, Buhrman RA, Myers EB, Ralph DC (2000) Current-driven magnetization reversal and spin-wave excitations in Co/Cu/Co pillars. Phys Rev Lett 84:3149–3152
86. Zhu JG, Kim N, Zhou Y, Zheng Y, Chang J, Ju K, Zhu X, White RM (2004) Current induced noise in CPP spin valves. IEEE Trans Magn 40:2323–2325

DOI 10.1007/978-94-007-7604-3_35-1
© Springer Science+Business Media Dordrecht 2014

87. Katine JA, Fullerton EE (2008) Device implications of spin-transfer torques. J Magn Magn Mater 320:1217–1226
88. Smith N, Katine JA, Childress JR, Carey MJ (2005) Angular dependence of spin torque critical currents for CPP-GMR read heads. IEEE Trans Magn 41:2935–2940
89. Smith N, Katine JA, Childress JR, Carey MJ (2006) Thermal and spin-torque noise in CPP (TMR and/or GMR) read sensors. IEEE Trans Magn 42:114–119
90. Xiao J, Zangwill A, Stiles MD (2004) Boltzmann test of Slonczewski's theory of spin-transfer torque. Phys Rev B 70:172405
91. Takagishi M, Yamada K, Iwasaki H, Fuke HN, Hashimoto S (2010) Magnetoresistance ratio and resistance area design of CPP-MR film for 2–5 Tb/in$^2$ read sensors. IEEE Trans Magn 46:2086–2089
92. Bonyhard PI, Lee JK (1990) Magnetoresistive read magnetic recording head offtrack performance assessment. IEEE Trans Magn 26:2448–2450
93. Lee JK, Bonyhard PI (1990) A track density model for magnetoresistive heads considering erase bands. IEEE Trans Magn 26:2475–2477
94. Jin Z, Salo M, Wood R (2008) Areal-density capability of a magnetic recording system using a "747" test based only on data-block failure-rate. IEEE Trans Magn 44:3718–3721
95. Uesugi T, Machita T, Miura S, Degawa N, Yamane T, Ohta M, Makino K, Kawasaki S, Hatate H, Nishizawa T, Kanaya T, Kagami T, Oike T (2013) Study of side shielded reader for future ultra-high TPI magnetic recording, TMRC 2013
96. Wood R, Williams M, Kavic A, Miles J (2009) The feasibility of magnetic recording at 10 terabits per square inch on conventional media. IEEE Trans Magn 45:917
97. Elidrissi MR, Chan KS, Yuan Z (2014) A study of DMR/TDMR with a double/triple reader head. IEEE Trans Magn 3:3100507
98. Valet T, Fert A (1993) Theory of the perpendicular magnetoresistance in magnetic multilayers. Phys Rev B 48:7099–7113
99. Pratt WP, Lee SF, Holody P, Yang Q, Loloee R, Bass J, Schroeder PA (1993) Giant magnetoresistance with current perpendicular to the multilayer planes. J Magn Magn Mater 126:406–409
100. Lee SF, Pratt WP, Yang Q, Holody P, Loloee R, Schroeder PA, Bass J (1993) Two-channel analysis of CPP-GMR data for AG/Co and AgSn/Co multilayers. J Magn Mag Mater 118:L1–L5
101. Piraux L, Dubois S, Fert A (1996) Perpendicular giant magnetoresistance in magnetic multilayered nanowires. J Magn Magn Mater 159:L287–L292
102. Jogo A, Nagasaka K, Ibusuki T, Shimizu Y, Tanaka A, Oshima H (2007) Current-perpendicular spin valves with high-resistivity ferromagnetic metals for ultrahigh-density magnetic recording. J Magn Magn Mater 309:80–86
103. Jiang Y, Abe S, Nozaki T, Tezuka N, Inomata K (2003) Perpendicular giant magnetoresistance and magnetic switching properties of a single spin valve with a synthetic antiferromagnet as a free layer. Phys Rev B 68:224426
104. Yuasa H, Fukuzawa H, Iwasaki H, Sahashi M (2005) The number of Cu lamination effect on current-to-plane giant-magnetoresistance of spin-valves with $Co_{50}Fe_{50}$ alloy. J Appl Phys 97:113907
105. Nikolaev K, Anderson P, Kolbo P, Dimitrov D, Xue S, Peng X, Pokhil T, Cho H, Chen Y (2008) Heusler alloy based current-perpendicular-to-the-plane giant magnetoresistance heads for high density magnetic recording. J Appl Phys 103(07):F533
106. Childress JR, Carey MJ, Maat S, Smith N, Fontana RE, Druist D, Carey K, Katine JA, Robertson N, Boone TD, Alex M, Moore J, Tsang CH (2008) All-metal current-perpendicular-

DOI 10.1007/978-94-007-7604-3_35-1
© Springer Science+Business Media Dordrecht 2014

to-plane giant magnetoresistance sensors for narrow-track magnetic recording. IEEE Trans Magn 44:90–93

107. Carey MJ, Maat S, Chandrashekariaih S, Katine JA, Chen W, York B, Childress JR (2011) $Co_2$ MnGe-based current-perpendicular-to-the-plane giant magnetoresistance spin-valve sensors for recording head applications. J Appl Phys 109:093912
108. Maat S, Carey MJ, Childress JR (2008) Current perpendicular to the plane spin-valves with CoFeGe magnetic layers. Appl Phys Lett 93:143505
109. Nakatani TM, Furubayashi T, Hono K (2011) Interfacial resistance and spin-dependent scattering in the current-perpendicular-to-plane giant magnetoresistance using $Co_2Fe(Al_{0.5}Si_{0.5})$ Heusler alloy and Ag. J Appl Phys 109:07B724
110. Sato J, Oogane M, Naganuma H, Ando Y (2011) Large magnetoresistance effect in epitaxial $Co_2Fe_{0.4}Mn_{0.6}Si/Ag/Co_2Fe_{0.4}Mn_{0.6}Si$ devices. Appl Phys Express 4:113005
111. Kubota T, Tsunegi S, Oogane M, Mizukami S, Miyazaki T, Naganuma H, Ando Y (2009) Half-metallicity and Gilbert damping constant in $Co_2FexMn_{1-x}Si$ Heusler alloys depending on the film composition. Appl Phys Lett 94:122504
112. Lee H, Wang YHA, Mewes CKA, Butler WH, Mewes T, Maat S, York B, Carey MJ, Childress JR (2009) Magnetization relaxation and structure of CoFeGe alloys. Appl Phys Lett 95:082502
113. Mizukami S, Watanabe D, Oogane M, Ando Y, Miura Y, Shirai M, Miyazaki M (2009) Low damping constant for $Co_2FeAl$ Heusler alloy films and its correlation with density of states. J Appl Phys 105:07D306
114. Oogane M, Kubota T, Kota K, Mizukami S, Naganuma H, Sakuma A, Ando Y (2010) Gilbert magnetic damping constant of epitaxially grown Co-based Heusler alloy thin films. Appl Phys Lett 96:252501
115. Childress JR, Carey MJ, Cyrille MC, Carey K, Smith N, Katine JA, Boone TD, Driskill-Smith AAG, Maat S, Mackay K, Tsang CH (2006) Fabrication and recording study of all-metal dual-spin-valve CPP read heads. IEEE Trans Magn 42:2444–2446
116. Childress JR, Carey MJ, Kiselev SI, Katine JA, Maat S, Smith N (2006) Dual current-perpendicular-to-the-plane giant magnetoresistive sensors for magnetic recording heads with reduced sensitivity to spin-torque noise. J Appl Phys 99:08S305
117. Carey MJ, Smith N, Maat S, Childress JR (2008) High-output current-perpendicular to the plane giant magnetoresistance sensor with synthetic-ferrimagnet free layer and enhanced spin-torque critical currents. Appl Phys Lett 93:102509
118. Reidy SG, Cheng L, Bailey WE (2003) Dopants for independent control of precessional frequency and damping in $Ni_{81}Fe_{19}$ (50 nm) thin films. Appl Phys Lett 82:1254–1256
119. Maat S, Smith N, Carey MJ, Childress JR (2008) Suppression of spin torque noise in current perpendicular to the plane spin-valves by addition of Dy cap layers. Appl Phys Lett 93:103506
120. Fukuzawa H, Yuasa H, Hashimoto S, Koi K, Iwasaki H, Takagishi M, Tanaka Y, Sahashi M (2004) MR ratio enhancement by NOL current-confined-path structures in CPP spin valves. IEEE Trans Magn 40:2236–2238
121. Fukuzawa H, Yuasa H, Hashimoto S, Iwasaki H, Tanaka Y (2005) Large magnetoresistance ratio of 10 % by $Fe_{50}Co_{50}$ layers for current-confined-path current-perpendicular-to-plane giant magnetoresistance spin-valve films. Appl Phys Lett 87:082507
122. Nakamoto K, Hoshiya H, Katada H, Hoshino K, Yoshida N, Shiimoto M, Takei H, Sato Y, Hatatani M, Watanabe K, Carey M, Maat S, Childress J (2008) CPP–GMR heads with a current screen layer for 300 $Gb/in^2$ recording. IEEE Trans Magn 44:95–99

DOI 10.1007/978-94-007-7604-3_35-1
© Springer Science+Business Media Dordrecht 2014

123. Shimazawa K, Tsuchiya Y, Mizuno T, Hara S, Chou T, Miyauchi D, Machita T, Ayukawa T, Ichiki T, Noguchi K (2010) CPP-GMR film with ZnO-based novel spacer for future high-density magnetic recording. IEEE Trans Magn 56:1487–1490
124. Braganca PM, Gurney BA, Wilson BA, Katine JA, Maat S, Childress JR (2010) Nanoscale magnetic field detection using a spin torque oscillator. Nanotechnology 21:235202